

Maximum Palinstrophy Growth in 2D Incompressible Flows: Instantaneous Case

Diego Ayala and Bartosz Protas*

Department of Mathematics and Statistics, McMaster University
Hamilton, Ontario, L8S 4K1, Canada

June 14, 2022

Abstract

In this study we investigate the vortex structures which lead to the maximum possible growth of palinstrophy in two-dimensional incompressible flows on a periodic domain. It is shown that these questions are related to a broader research program concerning the problem of the finite-time singularity formation in the three-dimensional Navier-Stokes system. Such extreme vortex events are found systematically via numerical solution of suitable variational optimization problems. We identify several families of maximizing vortex states parameterized by their palinstrophy, palinstrophy and energy and palinstrophy and enstrophy. Evidence is shown that some of these families saturate estimates for the instantaneous rate of growth of palinstrophy obtained using rigorous methods of mathematical analysis, thereby demonstrating that this analysis is in fact sharp. In the limit of small palinstrophies the optimal vortex states are found analytically, whereas for large palinstrophies they exhibit a self-similar multipolar structure. It is also shown that the time evolution obtained using some families of the instantaneously optimal states as the initial conditions saturates the theoretical upper bound for the maximum growth of palinstrophy in finite time. Possible consequences of this finding for the study of extreme events in fluid flows are discussed.

Keywords: 2D Navier-Stokes equation, maximum growth, palinstrophy, variational optimization, vortex dynamics

1 Introduction

This work makes a contribution to a broader research effort concerning systematic characterization of extreme events in hydrodynamic systems. In addition to their independent physical interest, such questions are intrinsically related to the problem of finite-time singularity formation in various flow models, which is one of the issues at the

*Email address for correspondence: bprotas@mcmaster.ca

center of mathematical fluid mechanics. In the context of the three-dimensional (3D) Navier-Stokes system in an unbounded or periodic domain, the key problem concerns the existence for arbitrarily large times of smooth solutions corresponding to arbitrary initial data (Doering, 2009). To date, global in time existence has been established for weak solutions only, which need not be smooth. On the other hand, for initial data of arbitrary size, smooth (classical) solutions are guaranteed to exist up to certain finite times only, and loss of regularity, referred to as “blow-up”, cannot be ruled out. The importance of this issue has been recognized by the Clay Mathematical Institute which identified it as one of the “millennium challenges” for the mathematics community with a suitable monetary prize (Fefferman, 2000). Similar questions concerning existence of smooth solutions also pertain to the Euler equations in 3D. While the problem is essentially one of mathematical analysis, a number of computational investigations have been undertaken (e.g., Brachet *et al.*, 1983; Brachet, 1991; Kerr, 1993; Hou, 2009; Pelz, 2001; Ohkitani & Constantin, 2008; Ohkitani, 2008; Grafke *et al.*, 2008; Gibbon *et al.*, 2008; Orlandi *et al.*, 2012), to understand whether or not blow-up may occur in finite time. Although some of these studies indicated the possibility of a blow-up, the results obtained to date are not conclusive and their interpretation remains the subject of a debate. Another related research direction involves the study of complex-valued extensions of the Euler and Navier-Stokes equations. The idea is that solutions to the equations which at some fixed time are real-analytic functions of the space variables possess singularities in the complex plane, and the distance from the real axis to the nearest singularity, referred to as the width of the analyticity strip (Sulem *et al.*, 1983), further characterizes the smoothness of the solution. Therefore, migration of such complex-plane singularities towards the real line might be a signature of an approaching blow-up. In the context of this approach we only mention recent studies by Matsumoto *et al.* (2008) and Siegel & Caffisch (2009), and refer the reader to the references quoted therein for further details. A common limitation of these earlier attempts is that the candidates for blow-up (given in terms of the initial data for the Navier-Stokes or Euler equations) were chosen in a rather ad-hoc manner based on some heuristic arguments. A long-term goal of the present research program is to conduct the search for potential finite-time singularities in hydrodynamic systems more systematically, leveraging modern methods of numerical optimization.

In mathematical analysis there are many different lines of attack on the Navier-Stokes regularity problem. One important approach relies on estimates for the growth of the *enstrophy* $\mathcal{E}(t) := \frac{1}{2} \int_{\Omega} |\nabla \times \mathbf{u}(t, \mathbf{x})|^2 d\Omega$, where $\mathbf{u}(t, \cdot) : \Omega \rightarrow \mathbb{R}^3$ is the velocity field and Ω is a 3D domain (periodic or unbounded). It is well known (Foias & Temam, 1989) that the loss of regularity will manifest itself by the enstrophy becoming unbounded $\mathcal{E}(t) \rightarrow \infty$ as $t \rightarrow t_0$, where t_0 is the blow-up time. Therefore, it is essential to provide tight bounds on how rapidly the enstrophy can grow, and the sharpest estimate available to date for the 3D Navier-Stokes system has the form (Doering, 2009)

$$\frac{d\mathcal{E}(t)}{dt} \leq \frac{27C^3}{32\nu^3} \mathcal{E}(t)^3, \quad (1)$$

where ν is the kinematic viscosity and $C > 0$ is a constant (hereafter C will denote a generic positive constant which may assume different numerical values in different instances). Since upon integration with respect to time this upper bound blows up at $t_0 = \frac{16\nu^3}{27C^3\mathcal{E}_0^2}$, where \mathcal{E}_0 is the initial value of the enstrophy, the regularity problem can be rephrased as the question whether or not estimate (1) can be saturated uniformly during the system evolution over a *finite* window of time $[0, T]$, where $T < t_0$. In other words, the question is whether there exists initial data \mathbf{u}_0 with some prescribed enstrophy \mathcal{E}_0 such that the corresponding system evolution will realize estimate (1) over a finite time window $[0, T]$. Such initial data can be sought via solution of a suitably formulated variational optimization problem for partial differential equation (PDEs) in which the objective is to maximize the growth of the enstrophy.

In order to investigate the possibility of a finite-time blow-up, two questions need to be addressed, namely:

- (P1) Sharpness of *instantaneous* estimate (1), and
- (P2) the maximum growth of enstrophy over *finite time* window $[0, T]$, which is mathematically defined as

$$\max_{\mathbf{u}_0 \in H^1(\Omega)} \mathcal{E}(T) \quad \text{subject to} \quad \mathcal{E}(0) = \mathcal{E}_0. \quad (2)$$

By solving optimization problem (2) over a set of time windows with increasing length T one could assess whether or not the worst-case growth of enstrophy indeed exhibits a tendency towards blow-up in finite time. Moreover, this will also shed light on the structure of the most singular initial data which can lead to new conjectures in the mathematical analysis of the problem. In the context of the 3D Navier-Stokes system problem P1 was already addressed in the seminal study by Lu & Doering (2008) (see also Lu, 2006), where it was demonstrated using computations that estimate (1) is in fact sharp (up to a prefactor). From the computational point of view, solution of problems P1 and P2 is based on a form of the discrete gradient flow. Needless to say, this approach is much more complicated in the case of open problem P2, since in order to compute the gradient directions, the time-dependent Navier-Stokes system and its suitably defined adjoint have to be solved. While this is a formidable computational task, it does appear within reach of the computational techniques and resources available to date. At this point it should be made clear that, although solving problem P2 is the long-term objective of the present research program, accomplishing this task will not resolve the Clay Millennium Problem where a rigorous mathematical proof is required (Fefferman, 2000).

Questions parallel to problems P1 and P2 can also be formulated in regard to the two-dimensional (2D) Navier-Stokes and one-dimensional (1D) Burgers equations. While for both of these systems it is well known that smooth solutions exist *globally* in time for arbitrary smooth initial data (Kreiss & Lorenz, 2004), one can also obtain estimates for both the instantaneous and finite-time growth of the relevant quadratic quantities and it

is important to know whether these estimates are sharp and can be attained during the nonlinear evolution of the system. Our interest is justified by the fact that these estimates are obtained using similar techniques as employed in the analysis of the 3D Navier-Stokes problem. The quantities of interest are the “enstrophy” $\mathcal{E}(t) := \frac{1}{2} \int_0^1 (\partial_x v(t, x))^2 dx$ in 1D, where $v : \mathbb{R}^+ \times [0, 1] \rightarrow \mathbb{R}$ is the solution of the Burgers equation, and the palinstrophy $\mathcal{P}(t) := \frac{1}{2} \int_\Omega |\nabla \omega(t, \mathbf{x})|^2 d\Omega$ in 2D, where $\Omega := [0, 1] \times [0, 1]$ and $\omega : \mathbb{R}^+ \times \Omega \rightarrow \mathbb{R}$ is the scalar vorticity (as will be discussed further below, enstrophy is not interesting in 2D, since in the absence of any right-hand side forcing, it can only decrease in flows on periodic and unbounded domains). The best estimates available to date for problems analogous to problems P1 and P2 for the 1D Burgers and 2D Navier-Stokes systems, together with the aforementioned results for the 3D Navier-Stokes system, are summarized in table 1. Determining whether or not the estimates listed in table 1 are sharp and, if so, identifying the solutions which saturate these estimates constitutes the long-term goal of this research program. In fact, significant progress has already been made addressing some of these questions. The instantaneous bound on $d\mathcal{E}/dt$ for the 1D Burgers problem was shown to be sharp by Lu & Doering (2008) (see also Lu, 2006), and a remarkable feature of this result is that it was obtained analytically. Finite-time estimates for the 1D Burgers problem were probed computationally by Ayala & Protas (2011), where it was shown that they are not in fact sharp. This result is important, as it suggests that the standard way for performing analysis based on integrating (sharp) instantaneous bounds over time might not be optimal and might lead to significant overestimates. The results obtained numerically by Ayala & Protas (2011) were then justified rigorously by Pelinovsky (2012*a,b*). We add here that variational optimization methods have recently been employed to study other fundamental problems in hydrodynamics involving the growth of quadratic quantities, such as for example optimal perturbations in the laminar-turbulent transition (Rabin *et al.*, 2012).

In this study we report new results concerning the sharpness of the instantaneous bounds on $d\mathcal{P}/dt$ in the 2D Navier-Stokes problem. Given the structure of the corresponding extremal vortex states, these results are also quite interesting from the physical point of view, outside the context of the singularity formation problem. Investigation of the bounds on the finite-time palinstrophy growth $\max_{t>0} \mathcal{P}(t)$ in the 2D Navier-Stokes problem is already under way and will be reported in the near future. Finding 3D flow fields with the largest possible growth of enstrophy in finite time remains an open problem to be addressed in the future research.

The structure of the paper is as follows: in the next section we discuss a number of rigorous estimates of the palinstrophy growth in the 2D Navier-Stokes system. In section 3 we demonstrate how questions about the sharpness of these estimates can be framed in terms of suitable variational optimization problems. A gradient-based approach to solution of such problems is discussed in section 4, whereas some analytical insights concerning the solutions of the maximization problems in the limit of small palinstrophies are presented in section 5. Computational results are presented in section 6 and discussed in section 7. Conclusions and a discussion of some future research directions are deferred to section 8. Some technical material is collected in an appendix.

	BEST ESTIMATE	SHARPNESS
1D Burgers instantaneous	$\frac{d\mathcal{E}}{dt} \leq \frac{3}{2} \left(\frac{1}{\pi^2\nu}\right)^{1/3} \mathcal{E}^{5/3}$	YES (Lu & Doering, 2008)
1D Burgers finite-time	$\max_{t \in [0, T]} \mathcal{E}(t) \leq \left[\mathcal{E}_0^{1/3} + \frac{1}{16} \left(\frac{1}{\pi^2\nu}\right)^{4/3} \mathcal{E}_0 \right]^3$	No (Ayala & Protas, 2011)
2D Navier-Stokes instantaneous	$\frac{d\mathcal{P}(t)}{dt} \leq -\nu \frac{\mathcal{P}^2}{\mathcal{E}} + \frac{C_1}{\nu} \mathcal{E} \mathcal{P}$ $\frac{d\mathcal{P}(t)}{dt} \leq \frac{C_2}{\nu} \mathcal{K}^{1/2} \mathcal{P}^{3/2}$	present work
2D Navier-Stokes finite-time	$\max_{t>0} \mathcal{P}(t) \leq \mathcal{P}_0 + \frac{C_1}{2\nu^2} \mathcal{E}_0^2$ $\max_{t>0} \mathcal{P}(t) \leq \left(\mathcal{P}_0^{1/2} + \frac{C_2}{4\nu^2} \mathcal{K}_0^{1/2} \mathcal{E}_0 \right)^2$	present work
3D Navier-Stokes instantaneous	$\frac{d\mathcal{E}(t)}{dt} \leq \frac{27C^2}{32\nu^3} \mathcal{E}(t)^3$	YES (Lu & Doering, 2008)
3D Navier-Stokes finite-time	$\mathcal{E}(t) \leq \frac{\mathcal{E}(0)}{\sqrt{1 - 4\frac{C\mathcal{E}(0)^2}{\nu^3}t}}$???

Table 1: Summary of the best estimates available to date for the instantaneous rate of growth and the growth over finite time of enstrophy and palinstrophy in 1D Burgers, 2D and 3D Navier-Stokes systems.

2 Two-Dimensional Navier-Stokes System

We consider a viscous incompressible fluid on a 2D periodic domain $\Omega = [0, 1] \times [0, 1]$. Its motion is governed by the Navier-Stokes equation, written here in the form

$$\frac{\partial \omega}{\partial t} + J(\omega, \psi) = \nu \Delta \omega \quad \text{in } (0, \infty) \times \Omega, \quad (3a)$$

$$-\Delta \psi = \omega \quad \text{in } (0, \infty) \times \Omega, \quad (3b)$$

$$\omega(0) = \omega_0 \quad \text{in } \Omega, \quad (3c)$$

where ψ and ω are, respectively, the streamfunction and (scalar) vorticity, whereas ω_0 is the initial condition. In system (3) ν denotes the kinematic viscosity (assumed fixed), Δ is the Laplacian operator and $J(f, g) := \partial_x f \partial_y g - \partial_y f \partial_x g$, defined for $f, g : \Omega \rightarrow \mathbb{R}$, is the Jacobian determinant. Discussion concerning various aspects of formulation (3) can be found, for example, in Majda & Bertozzi (2002).

We are interested in studying the growth of the following quadratic quantities characterizing the evolution of system (3)

$$\text{kinetic energy} \quad \mathcal{K}(\psi(t)) = \frac{1}{2} \int_{\Omega} |\nabla \psi(t, \mathbf{x})|^2 d\Omega, \quad (4)$$

$$\text{enstrophy} \quad \mathcal{E}(\psi(t)) = \frac{1}{2} \int_{\Omega} (\Delta \psi(t, \mathbf{x}))^2 d\Omega, \quad (5)$$

$$\text{palinstrophy} \quad \mathcal{P}(\psi(t)) = \frac{1}{2} \int_{\Omega} |\nabla \Delta \psi(t, \mathbf{x})|^2 d\Omega \quad (6)$$

which, to simplify our analysis, are rewritten here in terms of streamfunction as the state variable. Without loss of generality, we will assume that the streamfunction fields have zero mean. As regards enstrophy (5), we note that multiplying (3a) by ω , integrating the resulting expression over Ω , performing integration by parts and making necessary simplifications, we arrive at

$$\frac{d\mathcal{E}}{dt} = -2\nu \mathcal{P} < 0 \quad (7)$$

which implies that, unlike in the dimension one or three, in 2D flows on periodic domains the enstrophy can only decrease. This result (which also holds on unbounded domains) is a consequence of the absence of the “vortex stretching” term in the 2D vorticity equation (3a). On the other hand, the phenomenon of stretching is observed (in the form of the last term on the right-hand side) in the evolution equation for the vorticity gradient $\nabla \omega$ which is obtained by applying the gradient operator ∇ to equation (3a)

$$\frac{\partial \nabla \omega}{\partial t} + (\mathbf{u} \cdot \nabla) \nabla \omega = \nu \Delta \nabla \omega + \nabla \omega \cdot \nabla \mathbf{u}. \quad (8)$$

For clarity, this equation is written using the velocity field $\mathbf{u} = \left[\frac{\partial \psi}{\partial y}, -\frac{\partial \psi}{\partial x} \right]^T$. Palinstrophy (6) is the quadratic quantity associated with equation (8), and a relation characterizing

its evolution in time is obtained by dotting equation (8) with $\nabla\omega$, integrating over Ω , then integrating by parts and simplifying

$$\frac{d\mathcal{P}(t)}{dt} = \int_{\Omega} J(\Delta\psi, \psi) \Delta^2\psi \, d\Omega - \nu \int_{\Omega} (\Delta^2\psi)^2 \, d\Omega =: \mathcal{R}_{\mathcal{P}}(\psi), \quad (9)$$

where the subscript \mathcal{P} indicates the value of the palinstrophy for which the expression is evaluated. We note that now, unlike in equation (7), the right-hand side (RHS) features a cubic term representing stretching in addition to the negative-definite dissipative term. We add that a slightly different, but equivalent, expression for $d\mathcal{P}/dt$ was also obtained by Tran & Dritschel (2006).

Since palinstrophy may exhibit nontrivial behavior, we now go on to discuss various rigorous bounds available for the palinstrophy rate of growth (9). The following estimate was recently obtained by Doering & Lunasin (2011)

$$\frac{d\mathcal{P}}{dt} \leq -\nu \frac{\mathcal{P}^2}{\mathcal{E}} + \frac{C_1}{\nu} \mathcal{E} \mathcal{P}. \quad (10)$$

A different estimate is derived in appendix A and has the form

$$\frac{d\mathcal{P}}{dt} \leq \frac{C_2}{\nu} \mathcal{K}^{\frac{1}{2}} \mathcal{P}^{\frac{3}{2}}, \quad (11)$$

We observe that, in comparison to the corresponding estimates available in 1D and in 3D, (see table 1), bounds (10) and (11) have a different structure, since the RHS expressions depend on *two* quadratic quantities, respectively, \mathcal{E} and \mathcal{P} in (10), and \mathcal{K} and \mathcal{P} in (11), rather than just one. As a matter of course, the second quantity (\mathcal{E} or \mathcal{K}) can be eliminated using Poincaré's inequality [$\mathcal{K} \leq (2\pi)^{-2} \mathcal{E} \leq (2\pi)^{-4} \mathcal{P}$] yielding

$$\frac{d\mathcal{P}}{dt} \leq \frac{C}{\nu} \mathcal{P}^2 \quad (12)$$

(transforming (10) into (12) also requires dropping the negative-definite quadratic term). We note that, since the only functions saturating Poincaré's inequality are the eigenfunctions of the Laplacian, sharpness may be lost when moving from (10) and (11) to (12). Establishing whether or not upper bounds (10), (11) and (12) are sharp, and determining the structure of the corresponding maximizing fields is the main goal of the present study.

We add that some other estimates for the rate of growth of palinstrophy were also derived in the literature. For example, the following upper bound was established by Tran & Dritschel (2006)

$$\frac{d\mathcal{P}}{dt} \leq C \frac{\|\omega\|_{H^2(\Omega)}}{\|\omega\|_{L_2(\Omega)}} (\|\omega\|_{L_{\infty}(\Omega)} \mathcal{E} - \mathcal{P}), \quad (13)$$

where $\|\cdot\|_{L_2(\Omega)}$, $\|\cdot\|_{L_{\infty}(\Omega)}$ and $\|\cdot\|_{H^2(\Omega)}$ denote different Lebesgue and Sobolev norms. We remark that upper bound (13) relies on the control of higher (second) derivatives of

vorticity through $\|\omega\|_{H^2(\Omega)}$ and is therefore less interesting for our purposes. Some early results were also obtained by Pouquet *et al.* (1975), whereas estimates for the rate of growth of palinstrophy in the presence of body forcing were studied by Dascaliuc *et al.* (2010).

As regards the maximum growth of palinstrophy over finite time, using estimate (10) Doering & Lunasin (2011) found that

$$\max_{t>0} \mathcal{P}(t) \leq \mathcal{P}(0) + \frac{C_1}{2\nu^2} \mathcal{E}(0)^2 \leq \mathcal{P}(0) + \frac{C_1}{8\pi^2\nu^2} \mathcal{P}(0)^2. \quad (14)$$

Similarly, it follows from estimate (11) that, cf. appendix A,

$$\max_{t>0} \mathcal{P}(t) \leq \left(\mathcal{P}^{1/2}(0) + \frac{C_2}{4\nu^2} \mathcal{K}^{1/2}(0) \mathcal{E}(0) \right)^2. \quad (15)$$

It is worth noticing that, although finite-time estimates (14) and (15) are obtained from two different instantaneous estimates, they both give the same power-law behavior in the limits $\mathcal{P}(0) \rightarrow 0$ and $\mathcal{E}(0) \rightarrow \infty$ (assuming that $\mathcal{K}(0)$ is fixed in (15)).

Aside from the questions concerning the sharpness of estimates (10)–(12), and their inherent relation to the blow-up problem discussed in Introduction, there is also independent interest in the structure of the vorticity fields leading to the maximum possible palinstrophy production because of their relevance for the enstrophy cascade in 2D turbulence. In fact, various processes related to the stretching of vorticity gradients described by equation (8) have already received some attention in the literature (e.g., Protas *et al.*, 1999).

3 Probing Sharpness of Estimates Using Variational Optimization

We now go on to discuss how the question of the sharpness of estimates (10), (11) and (12) can be framed in terms of solutions of suitably-defined optimization problems. Analogous questions pertaining to problems in 1D and 3D, cf. table 1, have already been addressed by Ayala & Protas (2011) and Lu & Doering (2008), respectively. As regards estimate (10), the approach consists in finding, for fixed values of $\mathcal{E} = \mathcal{E}_0$ and $\mathcal{P} = \mathcal{P}_0$, the streamfunction field $\tilde{\psi}_{\mathcal{E}_0, \mathcal{P}_0}$ which achieves the greatest rate of palinstrophy production $\mathcal{R}_{\mathcal{P}_0}(\tilde{\psi}_{\mathcal{E}_0, \mathcal{P}_0})$, and then studying how it depends on the parameters \mathcal{E}_0 and \mathcal{P}_0 to see whether or not this dependence follows the predictions of estimate (10) (the use of streamfunction ψ , rather than the vorticity or velocity field, as the control variable leads to a simpler formulation of the optimization problem). As regards estimates (11) and (12), the approach is the same, except that, respectively, $\mathcal{K} := \mathcal{K}_0$ and \mathcal{P} or just \mathcal{P} are fixed. Thus, we arrive at the following two optimization problems corresponding to

estimates (10) and (11)

$$\begin{aligned}\tilde{\psi}_{\mathcal{E}_0, \mathcal{P}_0} &= \arg \max_{\psi \in \mathcal{S}_{\mathcal{E}_0, \mathcal{P}_0}} \mathcal{R}_{\mathcal{P}_0}(\psi) \\ \mathcal{S}_{\mathcal{E}_0, \mathcal{P}_0} &= \left\{ \psi \in H^4(\Omega) : \frac{1}{2} \int_{\Omega} (\Delta \psi)^2 d\Omega = \mathcal{E}_0, \frac{1}{2} \int_{\Omega} |\nabla \Delta \psi|^2 d\Omega = \mathcal{P}_0 \right\},\end{aligned}\tag{16}$$

$$\begin{aligned}\tilde{\psi}_{\mathcal{K}_0, \mathcal{P}_0} &= \arg \max_{\psi \in \mathcal{S}_{\mathcal{K}_0, \mathcal{P}_0}} \mathcal{R}_{\mathcal{P}_0}(\psi) \\ \mathcal{S}_{\mathcal{K}_0, \mathcal{P}_0} &= \left\{ \psi \in H^4(\Omega) : \frac{1}{2} \int_{\Omega} |\nabla \psi|^2 d\Omega = \mathcal{K}_0, \frac{1}{2} \int_{\Omega} |\nabla \Delta \psi|^2 d\Omega = \mathcal{P}_0 \right\},\end{aligned}\tag{17}$$

where maximization is performed over the Sobolev space $H^4(\Omega)$ of doubly-periodic functions with square-integrable fourth-order derivatives (Adams & Fournier, 2005). This regularity requirement plays a key role in the solution of optimization problems (16)–(17) as it ensures that the expression for the rate of growth of palinstrophy $\mathcal{R}_{\mathcal{P}_0}(\psi)$, cf. (9), is well-defined. We remark that the pairs of constraints in problems (16) and (17) are not in fact independent and must satisfy Poincaré’s inequalities, i.e., $\mathcal{E}_0 \leq (2\pi)^{-2} \mathcal{P}_0$ and $\mathcal{K}_0 \leq (2\pi)^{-4} \mathcal{P}_0$. The maximization problem corresponding to estimate (12) then takes the form

$$\begin{aligned}\tilde{\psi}_{\mathcal{P}_0} &= \arg \max_{\psi \in \mathcal{S}_{\mathcal{P}_0}} \mathcal{R}_{\mathcal{P}_0}(\psi) \\ \mathcal{S}_{\mathcal{P}_0} &= \left\{ \psi \in H^4(\Omega) : \frac{1}{2} \int_{\Omega} |\nabla \Delta \psi|^2 d\Omega = \mathcal{P}_0 \right\}\end{aligned}\tag{18}$$

in which only one constraint is present (in view of the earlier remark, we note that fixing palinstrophy $\mathcal{P}(\psi) = \mathcal{P}_0$ also provides upper bounds, via the aforementioned Poincaré’s inequalities, on both enstrophy $\mathcal{E}(\psi)$ and energy $\mathcal{K}(\psi)$). As will be shown in the next Section, single-constraint problem (18) is in fact fairly straightforward to solve numerically given the isotropic nature of the constraint. On the other hand, two-constraint problems (16) and (17) are much harder to solve, since the maximizers are to be sought at the intersection of two nonlinear constraint manifolds which may have a fairly complicated structure, both locally and globally.

We note that, due to the presence of the cubic term in the expression for $\mathcal{R}_{\mathcal{P}_0}(\psi)$, cf. (9), optimization problems (16)–(18) may be nonconvex, and hence the presence of multiple local maxima may be expected. We remark here that rescaling the domain Ω by rational factors will lead to a trivial multiplicity of the optimizing solutions. To demonstrate this, we consider system (3) on a rescaled domain $\Omega_L := [0, L] \times [0, L]$, where $L > 0$. The new independent variables become $\boldsymbol{\xi} := L\mathbf{x} \in \Omega_L$ and $\tau := L^\beta t$ for some $\beta \in \mathbb{R}$, whereas the corresponding solution can be expressed as $\Psi(\tau, \boldsymbol{\xi}) := L^\alpha \psi(t(\tau), \mathbf{x}(\boldsymbol{\xi}))$ for some $\alpha \in \mathbb{R}$. Transforming system (3) to the new variables, we observe that its form remains unchanged, provided that $\alpha = 0$ and $\beta = 2$. This shows that $\tilde{\Psi}_{\mathcal{E}_0, \mathcal{P}_0} := \tilde{\psi}_{\mathcal{E}_0, \mathcal{P}_0}(\mathbf{x}(\boldsymbol{\xi}))$ is a solution of optimization problem (16) rescaled to the new domain Ω_L . In the particular case when $L = 1/2, 1/4, \dots$ the domain Ω_L is periodically embedded in Ω . In such situation the maximizers $\tilde{\Psi}_{\mathcal{E}_0, \mathcal{P}_0}$ are nothing, but higher-wavenumber copies

of the “main” maximizer $\tilde{\psi}_{\mathcal{E}_0, \mathcal{P}_0}$ and this trivial multiplicity of maximizing solutions will not be separately considered here.

4 Gradient-Based Solution of Maximization Problems

In this Section we describe key elements of the computational algorithm for the solution of maximization problems stated in Section 3. We do this in the spirit of the “optimize-then-discretize” approach (Gunzburger, 2003). Solutions of maximization problems (16), (17) and (18) are characterized by the first-order optimality condition

$$\mathcal{R}'_{\mathcal{P}_0}(\tilde{\psi}; \psi') + \sum_{i=1}^m \lambda_i \mathcal{Q}'_i(\tilde{\psi}; \psi') = 0 \quad \forall \psi' \in H^4(\Omega) \quad (19)$$

where

$$\begin{aligned} \mathcal{R}'_{\mathcal{P}_0}(\psi; \psi') &:= \lim_{\epsilon \rightarrow 0} [\mathcal{R}_{\mathcal{P}_0}(\psi + \epsilon \psi') - \mathcal{R}_{\mathcal{P}_0}(\psi)] \quad \text{and} \\ \mathcal{Q}'_i(\psi; \psi') &:= \lim_{\epsilon \rightarrow 0} [\mathcal{Q}_i(\psi + \epsilon \psi') - \mathcal{Q}_i(\psi)], \quad i = 1, \dots, m \end{aligned}$$

are the Gâteaux (directional) differentials (Luenberger, 1969) of, respectively, the objective function and the individual constraints $\mathcal{Q}_i(\psi)$ defining the manifolds $\mathcal{S}_{\mathcal{E}_0, \mathcal{P}_0}$, $\mathcal{S}_{\mathcal{K}_0, \mathcal{P}_0}$ and $\mathcal{S}_{\mathcal{P}_0}$, cf. (16), (17) and (18). The field ψ' represents an arbitrary direction of differentiation in the space $H^4(\Omega)$, and $\lambda_i \in \mathbb{R}$ are the Lagrange multipliers associated with the constraints \mathcal{Q}_i , $i = 1, \dots, m$ ($m = 2$ for problems (16) and (17), and $m = 1$ for problem (18)).

The maximizer $\tilde{\psi}$ can be found using the following iterative gradient-ascent algorithm which can be interpreted as a discretization of a continuous gradient flow

$$\begin{aligned} \tilde{\psi} &= \lim_{n \rightarrow \infty} \psi^{(n)} \\ \psi^{(n+1)} &= \mathbb{P}\mathcal{S} \left(\psi^{(n)} + \tau_n \nabla \mathcal{R}_{\mathcal{P}}(\psi^{(n)}) \right) \\ \psi^{(1)} &= \psi_0, \end{aligned} \quad (20)$$

where $\psi^{(n)}$ is the approximation of the maximizer $\tilde{\psi}$ obtained at the n -th iteration, ψ_0 is the initial guess, τ_n the length of the step and $\mathbb{P}\mathcal{S} : H^4 \rightarrow \mathcal{S}$ is the projection operator onto the constraint manifold \mathcal{S} (without subscripts, symbol \mathcal{S} denotes a generic manifold). We emphasize that the use of the projection $\mathbb{P}\mathcal{S}$ ensures that, at every step n in optimization iteration (20), the constraint $\psi^{(n)} \in \mathcal{S}$ is satisfied up to machine precision. From the computational point of view, such formulation is in fact preferred to the more standard approach based on Lagrange multipliers and projections onto the tangent space $T\mathcal{S}$ which involve linearization of the constraints and hence result in accumulation of errors.

A key ingredient of algorithm (20) is evaluation of the gradient $\nabla \mathcal{R}_{\mathcal{P}_0}$ of objective function $\mathcal{R}_{\mathcal{P}_0}(\psi)$, cf. (9), representing its (infinite-dimensional) sensitivity to perturbations of the streamfunction ψ . It is essential that the gradient be characterized by the

required regularity, namely, $\nabla \mathcal{R}_{\mathcal{P}_0}(\psi) \in H^4(\Omega)$. This is, in fact, guaranteed by Riesz representation theorem (Luenberger, 1969), applicable because the Gâteaux differential $\mathcal{R}'_{\mathcal{P}_0}(\psi; \cdot) : H^4(\Omega) \rightarrow \mathbb{R}$ is a bounded linear functional on $H^4(\Omega)$. Thus, we have

$$\mathcal{R}'_{\mathcal{P}_0}(\psi; \psi') = \left\langle \nabla \mathcal{R}_{\mathcal{P}_0}(\psi), \psi' \right\rangle_{H^4(\Omega)} = \left\langle \nabla^{L_2} \mathcal{R}_{\mathcal{P}_0}(\psi), \psi' \right\rangle_{L_2(\Omega)} \quad (21)$$

in which the Riesz representers $\nabla \mathcal{R}_{\mathcal{P}_0}(\psi)$ and $\nabla^{L_2} \mathcal{R}_{\mathcal{P}_0}(\psi)$ are the gradients computed with respect to the H^4 and L_2 topology, respectively. The corresponding inner products are defined as follows

$$\forall z_1, z_2 \in L_2(\Omega) \quad \left\langle z_1, z_2 \right\rangle_{L_2(\Omega)} = \int_{\Omega} z_1 z_2 d\Omega, \quad (22)$$

$$\begin{aligned} \forall z_1, z_2 \in H^4(\Omega) \quad \left\langle z_1, z_2 \right\rangle_{H^4(\Omega)} = & \int_{\Omega} z_1 z_2 + \ell_1^2 \nabla z_1 \cdot \nabla z_2 + \ell_2^4 \Delta z_1 \Delta z_2 \\ & + \ell_3^6 \nabla \Delta z_1 \cdot \nabla \Delta z_2 + \ell_4^8 \Delta^2 z_1 \Delta^2 z_2 d\Omega, \end{aligned} \quad (23)$$

where $\ell_1, \ell_2, \ell_3, \ell_4 \in \mathbb{R}$ are adjustable parameters with the meaning of length-scales (Protas *et al.*, 2004) and the choice of their numerical values will be discussed further below. We remark that while the H^4 gradient is used exclusively in the actual computations, cf. (20), the L_2 gradient is computed first as an intermediate step. Calculating the Gâteaux differential of $\mathcal{R}_{\mathcal{P}_0}(\psi)$ and identifying it with the L_2 inner product (22) we thus obtain

$$\begin{aligned} \mathcal{R}'_{\mathcal{P}_0}(\psi; \psi') &= \int_{\Omega} [\Delta^2 J(\Delta \psi, \psi) + \Delta J(\psi, \Delta^2 \psi) + J(\Delta^2 \psi, \Delta \psi) - 2\nu \Delta^4 \psi] \psi' d\Omega \\ &= \left\langle \nabla^{L_2} \mathcal{R}_{\mathcal{P}_0}(\psi), \psi' \right\rangle_{L_2(\Omega)} \end{aligned} \quad (24)$$

from which it follows that

$$\nabla^{L_2} \mathcal{R}_{\mathcal{P}_0}(\psi) = \Delta^2 J(\Delta \psi, \psi) + \Delta J(\psi, \Delta^2 \psi) + J(\Delta^2 \psi, \Delta \psi) - 2\nu \Delta^4 \psi. \quad (25)$$

Identifying the left-hand side (LHS) of (24) with the H^4 inner product (23), integrating by parts and using (25), we obtain the required H^4 gradient as the solution of the following elliptic boundary-value problem

$$\begin{aligned} [\text{Id} - \ell_1^2 \Delta + \ell_2^4 \Delta^2 - \ell_3^6 \Delta^3 + \ell_4^8 \Delta^4] \nabla \mathcal{R}_{\mathcal{P}_0} &= \nabla^{L_2} \mathcal{R}_{\mathcal{P}_0} \quad \text{in } \Omega, \\ \text{Periodic Boundary Conditions.} \end{aligned} \quad (26)$$

As shown by Protas *et al.* (2004), extraction of gradients in spaces of smoother functions such as $H^4(\Omega)$ can be interpreted as low-pass filtering of the L_2 gradients with parameters $\ell_1, \ell_2, \ell_3, \ell_4$ acting as a cut-off length-scales.

The step size τ_n in algorithm (20) is calculated as

$$\tau_n = \arg \max_{\tau > 0} \left\{ \mathcal{R}_{\mathcal{P}} \left[\mathbb{P}\mathcal{S} \left(\psi^{(n)} + \tau \nabla \mathcal{R}_{\mathcal{P}}(\psi^{(n)}) \right) \right] \right\} \quad (27)$$

which is done using a derivative-free line search algorithm (Ruszczyński, 2006). Equation (27) can be interpreted as a modification of a standard line search method where the optimization is performed following an arc (a geodesic) lying on the constraint manifold \mathcal{S} , rather than a straight line. This approach was already successfully employed to solve a similar problem in Ayala & Protas (2011). The projection $\phi \mapsto \mathbb{P}\mathcal{S}(\phi)$ for some $\phi \in H^4(\Omega)$ is calculated by solving an optimization subproblem with form depending on the type of the constraint as follows.

- **Single Constraint:** problem (18) involves the constraint manifold

$$\mathcal{S}_{\mathcal{P}_0} = \left\{ \phi \in H^4(\Omega) : \frac{1}{2} \int_{\Omega} |\nabla \Delta \phi|^2 d\Omega = \mathcal{P}_0 \right\}. \quad (28)$$

Then, the projection operator $\mathbb{P}\mathcal{S}_{\mathcal{P}_0}$ is defined as

$$\mathbb{P}\mathcal{S}_{\mathcal{P}_0}(\phi) = \sqrt{\frac{\mathcal{P}_0}{\mathcal{P}(\phi)}} \phi. \quad (29)$$

- **$(\mathcal{E}_0, \mathcal{P}_0)$ -Constraint:** problem (16) involves the constraint manifold

$$\mathcal{S}_{\mathcal{E}_0, \mathcal{P}_0} = \left\{ \phi \in H^4(\Omega) : \frac{1}{2} \int_{\Omega} (\Delta \phi)^2 d\Omega = \mathcal{E}_0, \frac{1}{2} \int_{\Omega} |\nabla \Delta \phi|^2 d\Omega = \mathcal{P}_0 \right\}. \quad (30)$$

Then, the projection $\phi \mapsto \mathbb{P}\mathcal{S}_{\mathcal{E}_0, \mathcal{P}_0}(\phi)$ is computed as $\mathbb{P}\mathcal{S}_{\mathcal{E}_0, \mathcal{P}_0}(\phi) = \lim_{k \rightarrow \infty} \varphi^{(k)}$, where

$$\varphi^{(k+1)} = \varphi^{(k)} - \tau_k \nabla \mathcal{Q}(\varphi^{(k)}), \quad k = 1, 2, \dots, \quad (31a)$$

$$\varphi^{(1)} = \phi \quad (31b)$$

in which $\mathcal{Q}(\varphi) = \frac{1}{2} [\mathcal{P}(\varphi) - \mathcal{P}_0]^2$ and $\nabla \mathcal{Q}(\varphi)$ is the corresponding gradient. That is, the projection onto $\mathcal{S}_{\mathcal{E}_0, \mathcal{P}_0}$ is obtained by solving a single-constraint optimization problem with cost functional $\mathcal{Q}(\varphi)$ penalizing the deviation from the second constraint and the first constraint enforced using (29).

- **$(\mathcal{K}_0, \mathcal{P}_0)$ -Constraint:** problem (17) involves the constraint manifold

$$\mathcal{S}_{\mathcal{K}_0, \mathcal{P}_0} = \left\{ \phi \in H^4(\Omega) : \frac{1}{2} \int_{\Omega} |\nabla \phi|^2 d\Omega = \mathcal{K}_0, \frac{1}{2} \int_{\Omega} |\nabla \Delta \phi|^2 d\Omega = \mathcal{P}_0 \right\}. \quad (32)$$

In analogy to the $(\mathcal{E}_0, \mathcal{P}_0)$ -constraint, the projection onto $\mathcal{S}_{\mathcal{K}_0, \mathcal{P}_0}$ is obtained by solving a single-constraint optimization problem of the type (31) with cost functional $\mathcal{Q}(\varphi) = \frac{1}{2} [\mathcal{K}(\varphi) - \mathcal{K}_0]^2$.

We add that, since none of the manifolds defined in (28), (30) and (32) has the structure of a linear space, the projections defined above are not orthogonal.

Families of maximizers parameterized by their palinstrophy \mathcal{P}_0 are found by solving problems (16), (17) and (18) for values of \mathcal{P}_0 progressively incremented or decremented by $\pm\Delta\mathcal{P}_0$ and using the previously obtained maximizer $\tilde{\psi}_{\mathcal{P}_0}$ as the initial guess ψ_0 for $\psi_{\mathcal{P}_0\pm\Delta\mathcal{P}_0}$ in (20). In order to carry out an exhaustive search for all possible maximizing fields, this process was initiated in a variety of ways, including different random fields and closed-form solutions to the limiting problems described in the next section.

5 Solution of the Maximization Problems in the Limit of Small Palinstrophies

In this Section we investigate the structure of the maximizing solutions in the limiting cases when $\mathcal{P}_0 \rightarrow 0$ in (18), $\mathcal{P}_0 \rightarrow (2\pi)^2\mathcal{E}_0$ in (16) and $\mathcal{P}_0 \rightarrow (2\pi)^4\mathcal{K}_0$ in (17). To focus attention, we will consider optimal vorticity distributions in the form of periodic vortex lattices with 4-fold rotational symmetry, i.e., possessing the property $\psi(x, y) = -\psi(y, -x)$.

We begin the discussion by analyzing the single-constraint optimization problem (18) in the limit $\mathcal{P}_0 \rightarrow 0$. The Euler-Lagrange equation characterizing the solutions of this problem is, cf. (9),

$$\mathcal{G}(\psi) + 2\nu\Delta^4\psi + \lambda\Delta^3\psi = 0, \quad (33a)$$

$$\frac{1}{2} \int_{\Omega} (\nabla\Delta\psi)^2 d\Omega = \mathcal{P}_0, \quad (33b)$$

where $\lambda \in \mathbb{R}$ is the Lagrange multiplier associated with constraint (33b), equation (33a) is subject to the doubly-periodic boundary conditions and we denoted $\mathcal{G}(\psi) := \Delta^2 J(\Delta\psi, \psi) + \Delta J(\psi, \Delta^2\psi) + J(\Delta^2\psi, \Delta\psi)$. In order to obtain insights about the behavior of solutions (ψ, λ) of (33) in the limit $\mathcal{P}_0 \rightarrow 0$, we use the following series expansion

$$\psi = \psi_0 + \mathcal{P}_0^{1/2} \psi_1 + \mathcal{P}_0^1 \psi_2 + O(\mathcal{P}_0^{3/2}), \quad (34a)$$

$$\lambda = \lambda_0 + \mathcal{P}_0^{1/2} \lambda_1 + \mathcal{P}_0^1 \lambda_2 + O(\mathcal{P}_0^{3/2}). \quad (34b)$$

Introducing ansatz (34) in (33) and collecting terms proportional to different powers of $\mathcal{P}_0^{1/2}$, we obtain at the leading order

$$\mathcal{P}_0^0 : \quad 2\nu\Delta^4\psi_0 + \lambda_0\Delta^3\psi_0 = -\mathcal{G}(\psi_0), \quad (35a)$$

$$\frac{1}{2} \int_{\Omega} (\nabla\Delta\psi_0)^2 d\Omega = 0, \quad (35b)$$

from which it follows immediately that $\psi_0 \equiv 0$. Using this result, at the next order we

have

$$\mathcal{P}_0^{1/2} : \quad 2\nu\Delta^4\psi_1 + \lambda_0\Delta^3\psi_1 = 0, \quad (36a)$$

$$\frac{1}{2} \int_{\Omega} (\nabla\Delta\psi_1)^2 d\Omega = 1, \quad (36b)$$

where we note that the vanishing of the contribution from $\mathcal{G}(\psi)$ in (36a) is due to ψ_0 being identically zero. While continuing this process might lead to some interesting insights, for our present purposes it is in fact sufficient to truncate expansions (34) at the order $O(\mathcal{P}_0)$. The corresponding approximation of our objective function (9) thus becomes

$$\mathcal{R}_{\mathcal{P}_0} = -\mathcal{P}_0 \nu \int_{\Omega} (\Delta\psi_1)^2 d\Omega + O(\mathcal{P}_0^{3/2}). \quad (37)$$

As regards problem (36) defining (ψ_1, λ_0) , we note that, since for zero-mean functions defined on doubly-periodic domains, $\text{Ker}(\Delta^3) = \{0\}$, equation (36a) becomes an eigenvalue problem $\Delta\psi_1 = \lambda'_0\psi_1$, where $\lambda'_0 := -\lambda_0/(2\nu) < 0$. It can be shown via direct calculation that $\mathcal{R}_{\mathcal{P}_0} \approx 2\nu\lambda'_0\mathcal{P}_0$ as $\mathcal{P}_0 \rightarrow 0$, cf. (37), and we are therefore interested in the eigenfunctions associated with the largest, i.e., the least negative, eigenvalues. There are two distinct possibilities corresponding to different arrangements of vortices with 4-fold rotational symmetry in the domain Ω , namely (cf. figure 1),

- aligned arrangement where

$$\psi_{1,a}(x, y) = \frac{1}{4} \sin(2\pi p x) \sin(2\pi q y), \quad p = 1, 2, \dots \quad (38)$$

with the eigenvalue $\lambda'_0 = -8\pi^2 p^2$ which is maximized for $p = 1$ resulting in

$$\mathcal{R}_{\mathcal{P}_0} \approx -16\pi^2 \nu \mathcal{P}_0, \quad (39)$$

- staggered arrangement where

$$\psi_{1,s}(x, y) = \frac{1}{4} \sin[2\pi p(x + y)] \sin[2\pi p(x - y)], \quad p = 1/2, 1, 3/2, \dots \quad (40)$$

with the eigenvalue $\lambda'_0 = -16\pi^2 p^2$ which is maximized for $p = 1/2$ resulting in

$$\mathcal{R}_{\mathcal{P}_0} \approx -8\pi^2 \nu \mathcal{P}_0. \quad (41)$$

We therefore conclude that, while $\mathcal{R}_{\mathcal{P}_0}(\psi_1)$ is negative-definite for both arrangements, it assumes larger (i.e., less negative) values for the staggered configuration. To prove that ψ_1 is indeed a local maximizer of $\mathcal{R}_{\mathcal{P}_0}(\psi)$ in the limit $\mathcal{P}_0 \rightarrow 0$, rather than just a saddle point, it would be necessary to demonstrate the negative definiteness of the Hessian of $\mathcal{R}_{\mathcal{P}_0}(\psi)$ at ψ_1 . This, however, becomes technically complicated and we will not study it here. Computational results presented in section 6 provide evidence that

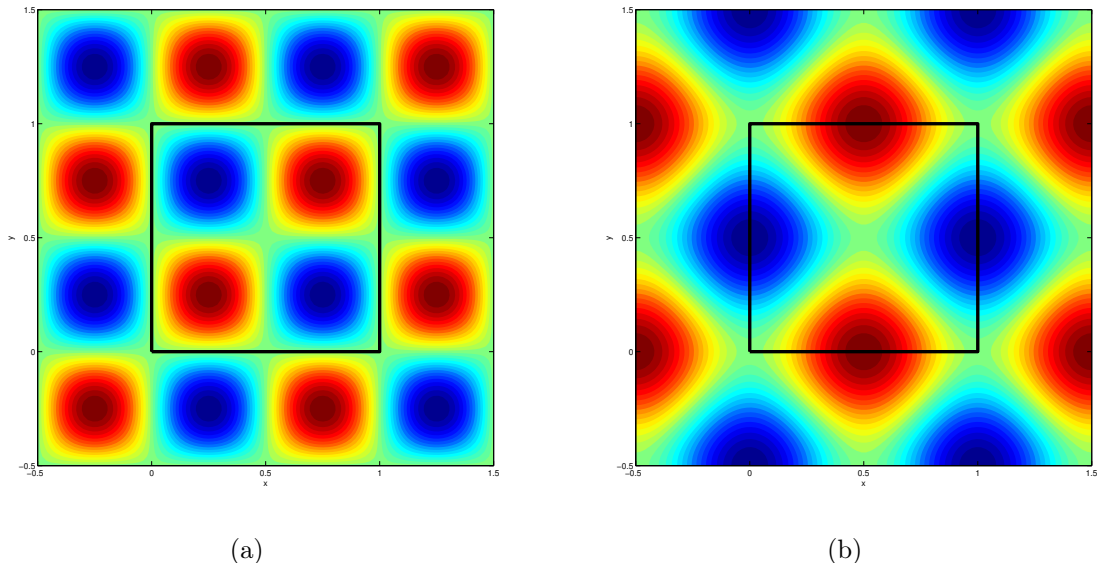


Figure 1: Vorticity fields characterized by (a) aligned and (b) staggered arrangement of vortex cells obtained as the solutions of maximization problem (18) in the limit $\mathcal{P}_0 \rightarrow 0$. They are given by, respectively, expressions (38) with $p = 1$ and (40) with $p = 1/2$. The boundary of the domain Ω is marked with the black solid line.

indeed the maximizers of the single-constraint problem (18) approach the field $\mathcal{P}_0^{1/2} \psi_1$ in the limit $\mathcal{P}_0 \rightarrow 0$. As regards the negativity of $\mathcal{R}_{\mathcal{P}_0}(\tilde{\psi}_{\mathcal{P}_0})$ in this limit, we remark that $J(\varphi, \Delta\varphi) \equiv 0$ when φ is an eigenfunction of the Laplacian and then the cubic part of $\mathcal{R}_{\mathcal{P}_0}(\tilde{\psi}_{\mathcal{P}_0})$ vanishes leaving just the dissipative terms.

As regards the two-constraint problems (16) and (17) in the respective limits $\mathcal{P}_0 \rightarrow (2\pi)^2 \mathcal{E}_0$ and $\mathcal{P}_0 \rightarrow (2\pi)^4 \mathcal{K}_0$, we note that, as the leading eigenfunction of the Laplacian, the maximizer $\psi_{1,s}$ defined in (40) saturates Poincaré's inequality, i.e., $\mathcal{P}(\psi_{1,s}) = (2\pi)^2 \mathcal{E}(\psi_{1,s})$. This means that second constraints $\mathcal{E}(\psi) = \mathcal{E}_0$ and $\mathcal{K}(\psi) = \mathcal{K}_0$ are satisfied automatically by $\psi_{1,s}$ and therefore need not be enforced through the introduction of another Lagrange multiplier. This allows us to conclude that $\psi_{1,s}$ is also the solution of the limiting forms of two-constraint optimization problems (16) and (17).

6 Computational Results

In the two subsections below we describe the results obtained from the numerical solution of optimization problems (18), (16) and (17) using the computational approaches described in Section 4 for a broad range of constraint parameters \mathcal{P}_0 , $(\mathcal{E}_0, \mathcal{P}_0)$ and $(\mathcal{K}_0, \mathcal{P}_0)$. In subsection 6.3 we discuss how the palinstrophy growth in finite time corresponding to the instantaneous maximizers found in Sections 6.1 and 6.2 used as the initial data compares with the available finite-time estimates.

In the calculations described in Sections 6.1 and 6.2 the key element is the evaluation of the gradient $\nabla \mathcal{R}_{\mathcal{P}_0}(\psi)$, first in the L_2 and then in the H^4 topology, cf. (25)–(26), which is done using a pseudospectral Fourier-Galerkin technique with standard dealiasing. The resolution varied from 128^2 to 1024^2 grid points in the low-palinstrophy and high-palinstrophy cases, respectively. Convergence of all calculations with respect to the grid refinement was carefully verified. The rate of convergence of discrete gradient flow (20) depends, among other factors, on the values of the length-scale parameters characterizing the Sobolev inner product (23). Based on our extensive numerical test, we used $\ell_1 = \ell_2 = 0$, $\ell_3 \in [10^{-2}, 10^{-1}]$ and $\ell_4 \in [10^{-4}, 10^{-2}]$ (with smaller values of ℓ_3 and ℓ_4 corresponding to higher numerical resolutions). In all calculations the value of the viscosity coefficient was $\nu = 10^{-3}$.

As regards the results for the time-dependent problem presented in Section 6.3, we used a numerical approach combining a standard pseudospectral discretization in space with the Krylov subspace method described by Edwards *et al.* (1994) for the time discretization to numerically solve system (3) for the vorticity evolution. As regards the initial data ω_0 , it was chosen as the vorticity corresponding to the solutions of optimization problems (16), (17) and (18), i.e., $-\Delta \tilde{\psi}_{\mathcal{E}_0, \mathcal{P}_0}$, $-\Delta \tilde{\psi}_{\mathcal{K}_0, \mathcal{P}_0}$ and $-\Delta \tilde{\psi}_{\mathcal{P}_0}$. In these simulations, the resolution varied from 512^2 to 4096^2 grid points depending on the characteristic length scales of the initial data which ensured that all calculations were well-resolved. Power-law exponents mentioned below were computed by fitting a linear polynomial to the $\log_{10}(d\mathcal{P}/dt)$ versus $\log_{10}(\mathcal{P}_0)$ relationship.

6.1 Optimization Problems with a Single Constraint on \mathcal{P}_0

In this section we discuss solutions of the single-constraint optimization problem (18) with the goal of assessing the sharpness of estimate (12). In figures 2(a) and 2(b) we show the maximum palinstrophy rate of growth $\mathcal{R}_{\mathcal{P}_0}(\tilde{\psi}_{\mathcal{P}_0})$ obtained, respectively, for small and large values of \mathcal{P}_0 . We note the presence of two distinct branches of maximizing solutions, and the corresponding vorticity fields $-\Delta \tilde{\psi}_{\mathcal{P}_0}$ are shown in figures 2(c,d,e) and 2(f,g,h). The two branches arise, via continuation with respect to parameter \mathcal{P}_0 , from the two limiting maximizers discussed in section 5 and characterized by the staggered and aligned arrangement of the vortex cells (cf. figure 1), with the latter case always giving a larger value of $\mathcal{R}_{\mathcal{P}_0}(\tilde{\psi}_{\mathcal{P}_0})$ for a given \mathcal{P}_0 . The localized vortex structure present in the field shown in figure 2(e) is magnified in figure 6(a). In agreement with the discussion in section 5, for small \mathcal{P}_0 the values of the maximum palinstrophy rate of growth $\mathcal{R}_{\mathcal{P}_0}(\tilde{\psi}_{\mathcal{P}_0})$ on both branches are negative and in the limit $\mathcal{P}_0 \rightarrow 0$ $\mathcal{R}_{\mathcal{P}_0}(\tilde{\psi}_{\mathcal{P}_0}) \sim -8\pi^2\nu\mathcal{P}_0$ and $\mathcal{R}_{\mathcal{P}_0}(\tilde{\psi}_{\mathcal{P}_0}) \sim -16\pi^2\nu\mathcal{P}_0$ in the two cases (figure 2(a)). On the other hand, in figure 2(b) we see that for large values of \mathcal{P}_0 the maximum rate of growth $\mathcal{R}_{\mathcal{P}_0}(\tilde{\psi}_{\mathcal{P}_0})$ exhibits a clear power-law behavior with respect to \mathcal{P}_0 for both branches. In both cases the exponent is 1.57 ± 0.05 which is less than the exponent 2 appearing in estimate (12), cf. table 2.

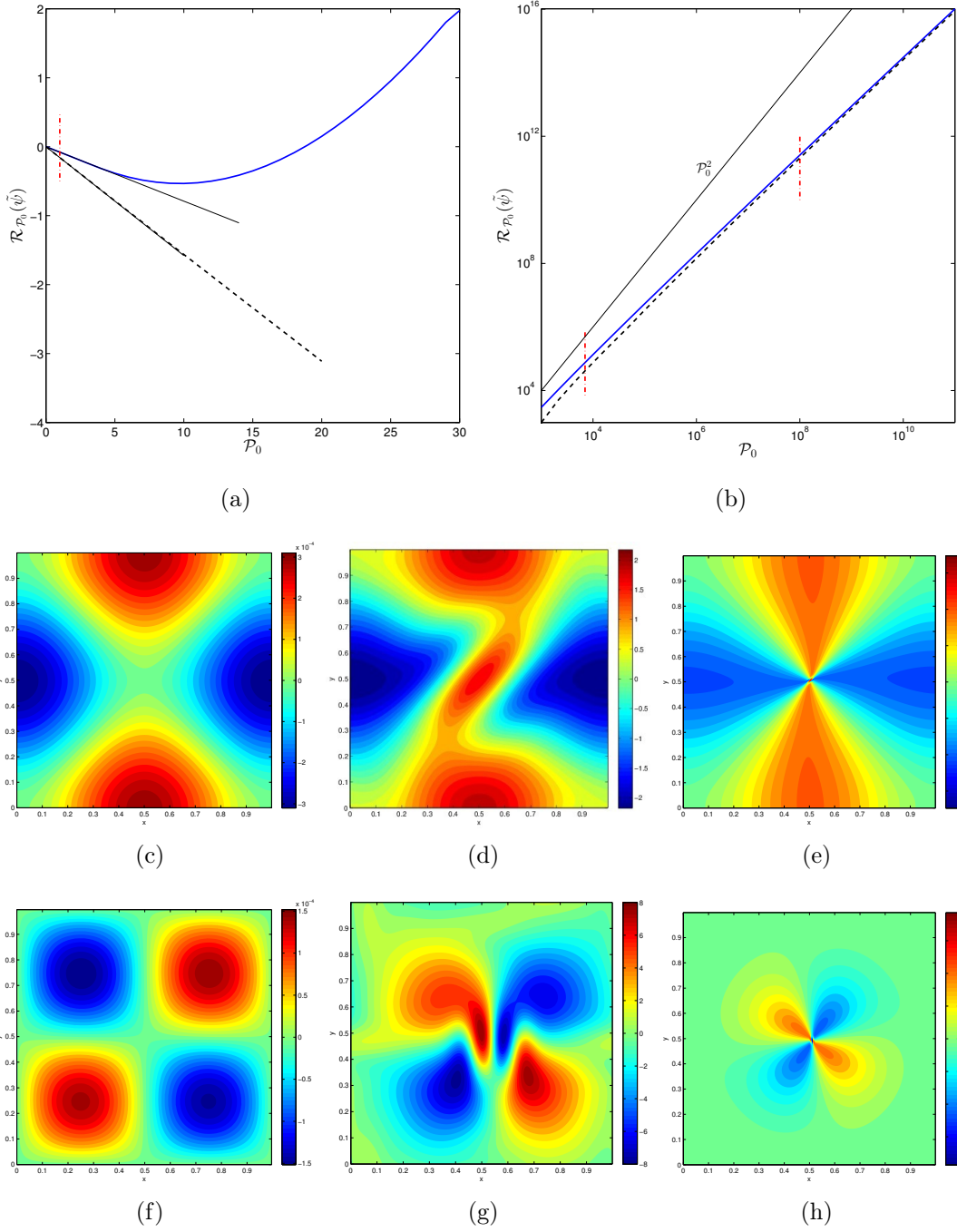


Figure 2: Dependence of the maximum palinstrophy rate of growth $\mathcal{R}_{\mathcal{P}_0}(\tilde{\psi}_{\mathcal{P}_0})$ on \mathcal{P}_0 for (a) small \mathcal{P}_0 and (b) large \mathcal{P}_0 ; (c–h) optimal vortex states corresponding to the branch with (c–e) staggered and (f–h) aligned arrangement of the vortex cells for the values of \mathcal{P}_0 marked with short vertical lines in figures (a) and (b); since the maximizing vortex states corresponding to the lower branch proved very difficult to compute accurately for intermediate values of \mathcal{P}_0 , this branch is not complete in figure (a).

6.2 Optimization Problems with Two Constraints on $(\mathcal{E}_0, \mathcal{P}_0)$ and $(\mathcal{K}_0, \mathcal{P}_0)$

We now discuss solutions of two-constraint optimization problems (16) and (17). In order to use these solutions to assess the sharpness of estimates (16) and (17), in both cases we present the results by fixing one of the constrained quantities, \mathcal{E}_0 or \mathcal{K}_0 , and then studying the maximum rate of growth of palinstrophy $\mathcal{R}_{\mathcal{P}_0}(\tilde{\psi}_{\mathcal{E}_0, \mathcal{P}_0})$ and $\mathcal{R}_{\mathcal{P}_0}(\tilde{\psi}_{\mathcal{K}_0, \mathcal{P}_0})$ as a function of the palinstrophy \mathcal{P}_0 which is allowed to vary over several orders of magnitude. The results are shown in figure 3(a) for $\mathcal{E}_0 = 100$ and in figure 4(a) for $\mathcal{K}_0 = 10$, each of which features two distinct solution branches representing the local maximizers. In both cases the values of the palinstrophy \mathcal{P}_0 for which the maximizing solutions are found are bounded from below by Poincaré's inequalities. In figures 3(c)–(h) and 4(c)–(h) we show the vorticity fields $-\Delta\tilde{\psi}_{\mathcal{E}_0, \mathcal{P}_0}$ and $-\Delta\tilde{\psi}_{\mathcal{K}_0, \mathcal{P}_0}$ corresponding to each of the two branches and different values of palinstrophy. We also remark that, as predicted in section 5, for small values of the palinstrophy \mathcal{P}_0 the maximizers $\tilde{\psi}_{\mathcal{E}_0, \mathcal{P}_0}$ and $\tilde{\psi}_{\mathcal{K}_0, \mathcal{P}_0}$ approach the Laplacian eigenfunctions given in (38) and (40), and the pairs of branches shown in Figures 3(a) and 4(a) correspond to the fields with the aligned and staggered arrangements of the “vortex cells”, cf. figure 1. The localized vortex structures present in the fields shown in figures 3(e) and 4(e) are magnified in figures 6(b,c). In figures 3(b) and 4(b) we present the maximum rate of growth of palinstrophy for a few different values of the first constraint, namely $\mathcal{E}_0 = 10^2, 10^3, 10^4$ and $\mathcal{K}_0 = 10^0, 10^1, 10^2$. For clarity, in these figures we only show the branches with higher values of $\mathcal{R}_{\mathcal{P}_0}$ which in both cases correspond to the maximizing fields with staggered vortex cells.

As is evident from figures 3(a,b) and 4(a,b), the two two-constraint problems lead to very different behavior of the maximum rate of growth of palinstrophy when $\mathcal{P}_0 \rightarrow \infty$. In the case with the $(\mathcal{K}_0, \mathcal{P}_0)$ -constraint it exhibits a clear power-law characterized by

$$\frac{d\mathcal{P}}{dt} \sim \mathcal{P}_0^{1.49 \pm 0.02} \quad (42)$$

which is consistent with estimate (11), thereby confirming its sharpness. On the other hand, the case with the $(\mathcal{E}_0, \mathcal{P}_0)$ -constraint reveals a sharp decrease of $d\mathcal{P}/dt$ observed for large values of \mathcal{P}_0 regardless of the value of \mathcal{E}_0 . It should be clarified, however, that this does not mean that the branches cannot be continued, but only that for sufficiently large values of \mathcal{P}_0 the corresponding values of $d\mathcal{P}/dt$ are negative and thus are not shown in a log-log plot. We emphasize that this behavior is in fact consistent with estimate (10) in which the increase of $d\mathcal{P}/dt$ is at large values of \mathcal{P}_0 limited by the negative-definite quadratic term. As shown in figure 3(a), this behavior is qualitatively captured by the dependence of $\mathcal{R}_{\mathcal{P}_0}(\tilde{\psi}_{\mathcal{E}_0, \mathcal{P}_0})$ on \mathcal{P}_0 .

6.3 Palinstrophy Growth in Finite Time

We consider solutions of Navier-Stokes system (3) with the following initial data

$$(i) \quad \omega_0 = -\Delta\tilde{\psi}_{\mathcal{P}_0},$$

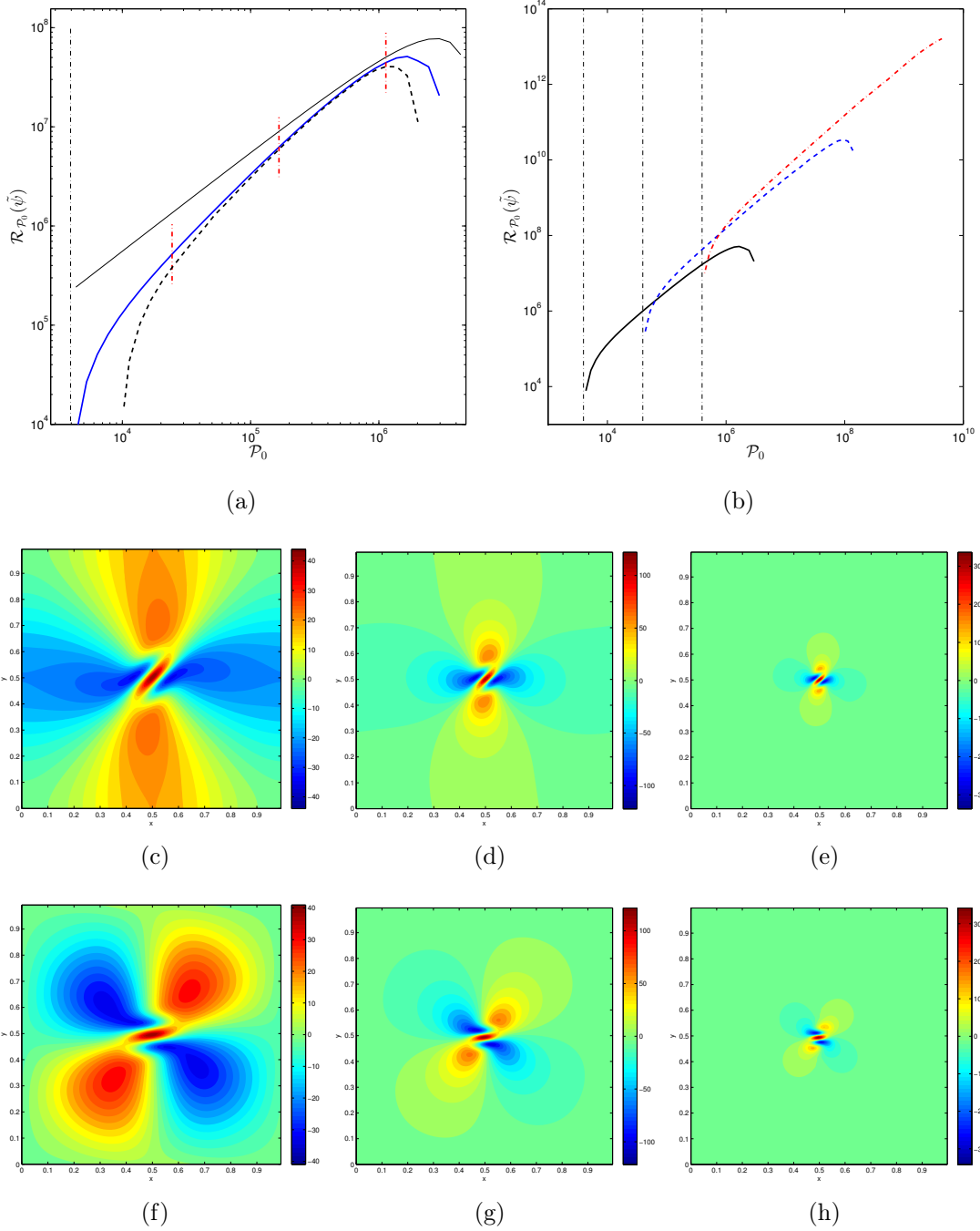


Figure 3: Dependence of the maximum palinstrophy rate of growth $\mathcal{R}_{P_0}(\tilde{\psi}_{\mathcal{E}_0, P_0})$ on P_0 for (a) $\mathcal{E}_0 = 100$ and (b) $\mathcal{E}_0 = 10^2, 10^3$ and 10^4 . Figure (a) shows both solution branches, whereas figure (b) only the ones with larger values of \mathcal{R}_{P_0} . Optimal vortex states corresponding to the two branches are shown in figures (c–e) and (f–h) for the following palinstrophy values: (c,f) $P_0 \approx 10\mathcal{P}_c$, (d,g) $P_0 \approx 10^2\mathcal{P}_c$ and (e,h) $P_0 \approx 10^3\mathcal{P}_c$ (marked with short vertical dashes), where $\mathcal{P}_c = (2\pi)^2\mathcal{E}_0$ is the Poincaré limit indicated with vertical dash-dotted lines in figures (a) and (b).

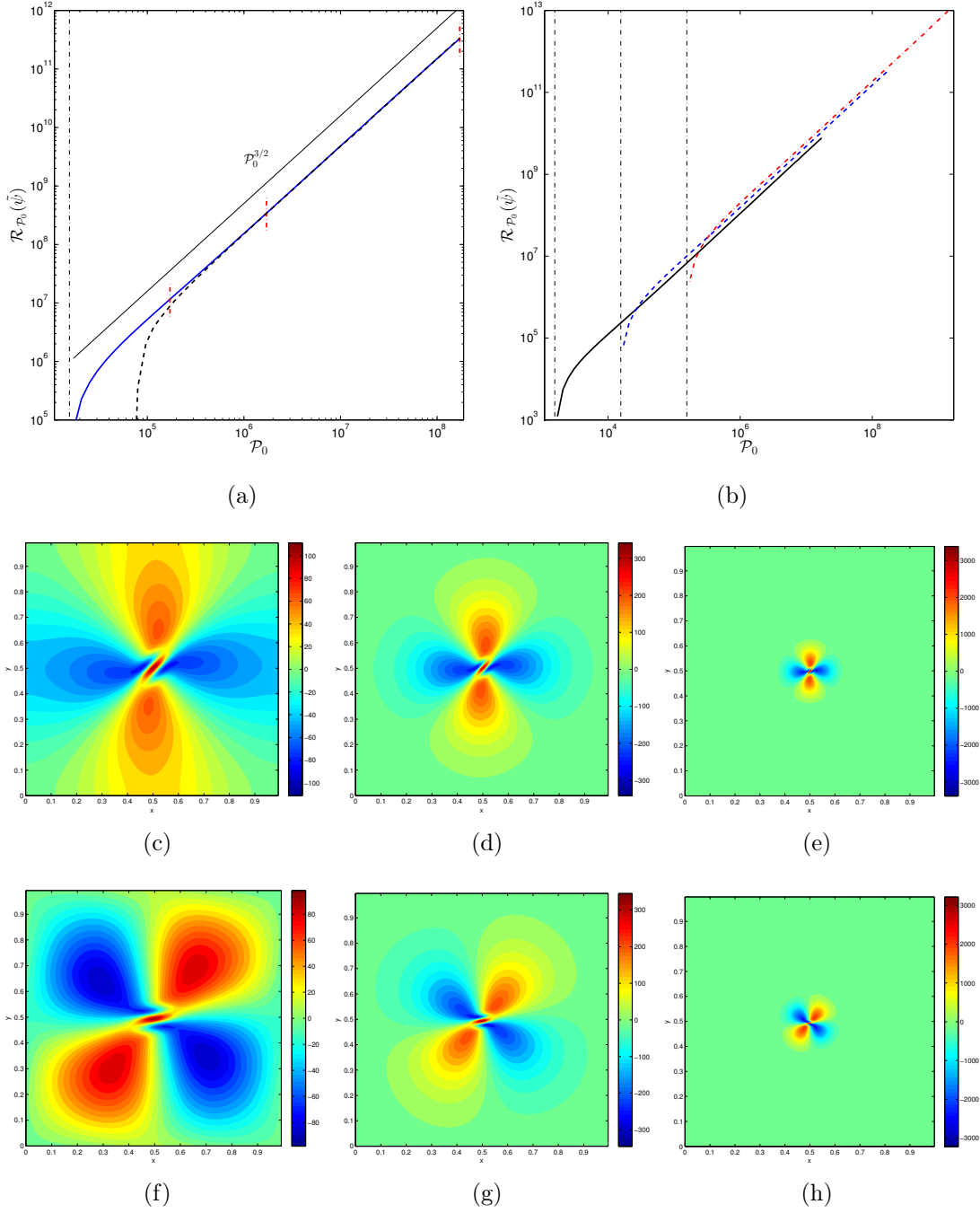


Figure 4: Dependence of the maximum palinstrophy rate of growth $\mathcal{R}_{\mathcal{P}_0}(\tilde{\psi}_{\mathcal{K}_0, \mathcal{P}_0})$ on \mathcal{P}_0 for (a) $\mathcal{K}_0 = 10$ and (b) $\mathcal{K}_0 = 10^0, 10^1$ and 10^2 . Figure (a) shows both solution branches, whereas figure (b) only the ones with larger values of $\mathcal{R}_{\mathcal{P}_0}$. Optimal vortex states corresponding to the two branches are shown in figures (c–e) and (f–h) for the following palinstrophy values: (c,f) $\mathcal{P}_0 = 10\mathcal{P}_c$, (d,g) $\mathcal{P}_0 = 10^2\mathcal{P}_c$ and (e,h) $\mathcal{P}_0 = 10^4\mathcal{P}_c$ (marked with short vertical dashes), where $\mathcal{P}_c = (2\pi)^4\mathcal{K}_0$ is the Poincaré limit indicated with vertical dash-dotted lines in figures (a) and (b).

$$(ii) \quad \omega_0 = -\Delta \tilde{\psi}_{\mathcal{K}_0, \mathcal{P}_0},$$

$$(iii) \quad \omega_0 = -\Delta \tilde{\psi}_{\mathcal{E}_0, \mathcal{P}_0}.$$

To obtain insights about the sharpness of finite-time estimates (14) and (15), we are interested in the maximum palinstrophy attained over time $\mathcal{P}_{\max} := \max_{t>0} \mathcal{P}(t)$ and its increment with respect to the initial value $\delta\mathcal{P} := \mathcal{P}_{\max} - \mathcal{P}_0$ as functions of the initial enstrophy \mathcal{E}_0 and palinstrophy \mathcal{P}_0 (the reason for studying $\delta\mathcal{P}$ is that the term \mathcal{P}_0 may mask the behavior of the other term on the RHS in (14) if it should also scale with an exponent close to the unity). Figure 5(a) shows $\delta\mathcal{P}$ for each case (i)–(iii) as a function of \mathcal{P}_0 with $\mathcal{K}_0 = 10$ in case (ii) and $\mathcal{E}_0 = 10^3$ in case (iii). These results exhibit a power-law behavior in cases (i) and (ii), whereas in case (iii) a sharp decrease of $\delta\mathcal{P}$ is observed as $\mathcal{P}_0 \rightarrow \infty$. The power laws for cases (i) and (ii) are

$$\begin{aligned} (i) \quad \delta\mathcal{P} &\sim \mathcal{P}_0^{1.13 \pm 0.03}, \\ (ii) \quad \delta\mathcal{P} &\sim \mathcal{P}_0^{1.05 \pm 0.09}. \end{aligned} \tag{43}$$

This behavior is parallel to the behavior reported in Sections 6.1 and 6.2 where power-law scaling was observed in the single-constraint problem and in the $(\mathcal{K}_0, \mathcal{P}_0)$ -constrained problem, but not in the $(\mathcal{E}_0, \mathcal{P}_0)$ -constrained problem. The exponents characterizing power laws (43) are significantly smaller than 2 predicted by estimate (14). The dependence of \mathcal{P}_{\max} on \mathcal{E}_0 in cases (i) and (ii) is shown in figure 5(b) (\mathcal{E}_0 rather than \mathcal{P}_0 is chosen as the abscissa, since this is the “independent variable” in the nonlinear term in estimate (15), and case (ii) is not shown, because in this configuration \mathcal{E}_0 is fixed). The following two distinct power laws are observed in the two cases

$$\begin{aligned} (i) \quad \mathcal{P}_{\max} &\sim \mathcal{E}_0^{1.17 \pm 0.02}, \\ (ii) \quad \mathcal{P}_{\max} &\sim \mathcal{E}_0^{1.98 \pm 0.07}, \end{aligned} \tag{44}$$

implying that the maximizing vortex states obtained under the $(\mathcal{K}_0, \mathcal{P}_0)$ -constraint lead to a finite-time palinstrophy evolution which *also* saturates the finite-time estimate (15). The significance of this finding will be discussed in more detail in the following section. An analysis of the corresponding time evolution of the vorticity field will be presented in a separate work (Ayala & Protas, 2013). Here, in figure 6(d), we only show the vorticity field at an instant of time when the palinstrophy maximum is achieved (it corresponds to $\omega_0 = -\Delta \tilde{\psi}_{\mathcal{K}_0, \mathcal{P}_0}$ with $\mathcal{K}_0 = 10$ and $\mathcal{P}_0 = 10^8$ used as the initial data in (3)). The exponents characterizing all the power laws discussed in this section are collected in table 2.

7 Discussion

In this Section we comment on some of the theoretical results introduced in Section 2 in the light of the findings presented in Section 6. Given their connection to the finite-time blow-up problem in 3D, our main interest here is establishing the sharpness

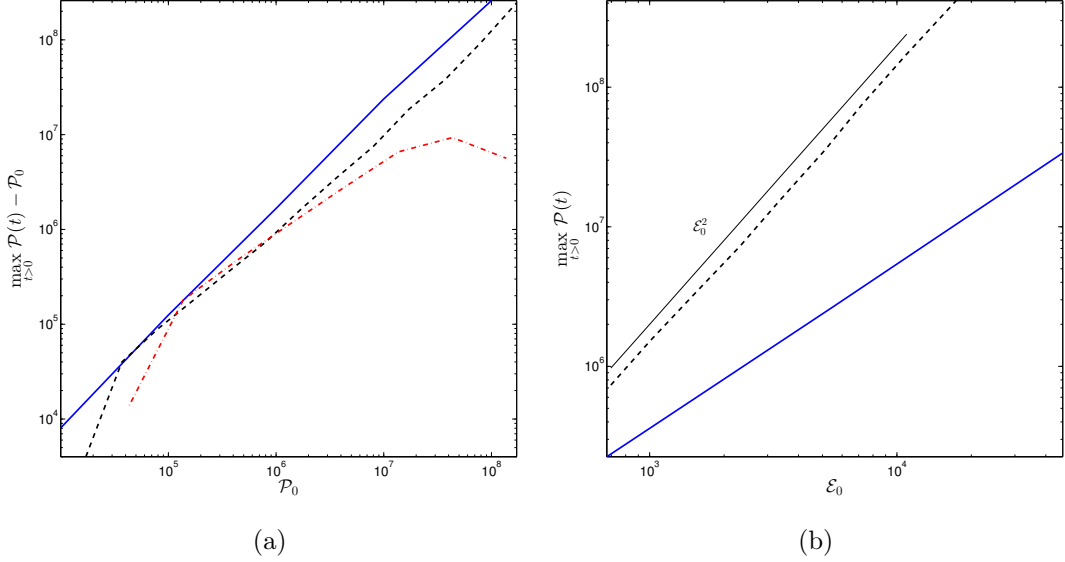


Figure 5: (a) $\delta\mathcal{P}$ as a function of initial palinstrophy \mathcal{P}_0 for (solid) case (i), (dashed) case (ii) and (dotted) case (iii); (b) \mathcal{P}_{\max} as a function of initial enstrophy \mathcal{E}_0 for (solid) case (i) and (dashed) case (ii); see text in section 6.3 for the definition of each case.

of estimates (10)–(12) for $d\mathcal{P}/dt$. From figures 4(a,b) and table 2 we see that solutions of optimization problem (17) lead to the growth of $\mathcal{R}_{\mathcal{P}_0}$ which saturates estimate (11) for sufficiently large \mathcal{P}_0 , and we therefore conclude that this estimate is sharp. As regards upper bound (10), due to the presence of the negative quadratic term, this estimate does not have the form of a power-law allowing for an arbitrary growth of $\mathcal{R}_{\mathcal{P}_0}(\tilde{\psi}_{\mathcal{E}_0, \mathcal{P}_0})$. This is indeed confirmed by the behavior of the solutions of optimization problem (16) shown in Figures 3(a,b) where we see that on each branch the quantity $\mathcal{R}_{\mathcal{P}_0}(\tilde{\psi}_{\mathcal{E}_0, \mathcal{P}_0})$ eventually decreases with \mathcal{P}_0 . Hence, in this case a power-law cannot be in fact defined. Since the qualitative features of estimate (10) are reproduced by the actual dependence of $\mathcal{R}_{\mathcal{P}_0}(\tilde{\psi}_{\mathcal{E}_0, \mathcal{P}_0})$ on \mathcal{P}_0 observed in figures 3(a,b), we can conclude that this estimate predicts the correct behavior, although in the absence of a power-law, it is hard to quantify this statement in terms of exponents. It is interesting that optimization problems (16) and (17) which have a rather similar structure lead to quite different global behavior of the maximizing solutions. The reason for this is that, as the palinstrophy \mathcal{P}_0 is increased, in the $(\mathcal{E}_0, \mathcal{P}_0)$ -constrained family of optimizers the energy $\mathcal{K}(\tilde{\psi}_{\mathcal{E}_0, \mathcal{P}_0})$ can not increase arbitrarily, as it is upper-bounded by \mathcal{E}_0 via Poincaré’s inequality. On the other hand, in the $(\mathcal{K}_0, \mathcal{P}_0)$ -constrained family of optimizers the constraint on \mathcal{K}_0 does not limit the growth of the enstrophy $\mathcal{E}(\tilde{\psi}_{\mathcal{K}_0, \mathcal{P}_0})$ of the maximizing solutions. In regard to the finite-time estimates, the fact that upper bound (14) is not saturated (figure 5(a)) was to be expected, given that the corresponding instantaneous estimate (10) was not sharp either. On the other hand, the fact that upper bound (15) is saturated

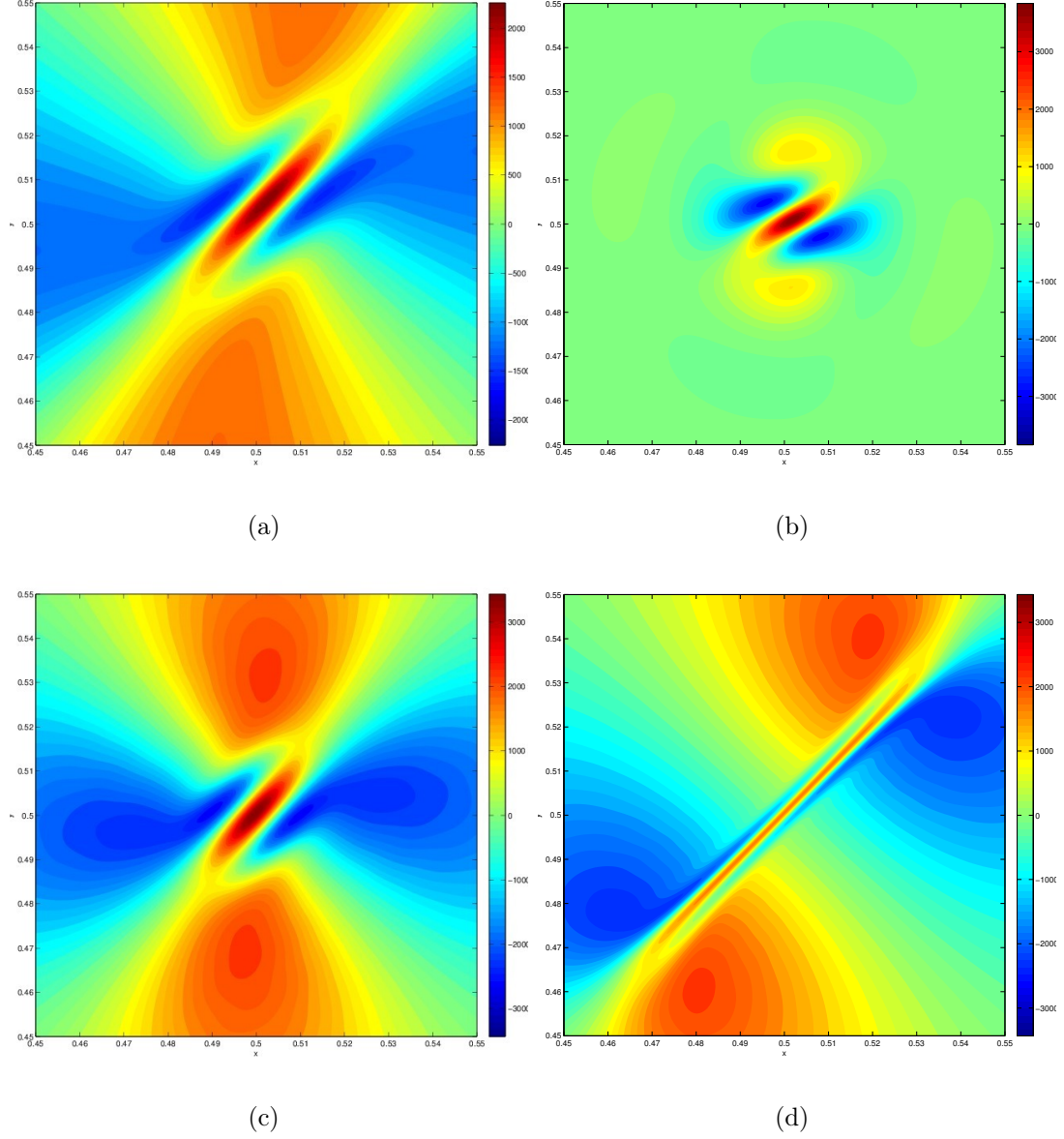


Figure 6: Magnifications of localized vortex structures present in the maximizing vorticity fields (a) $-\Delta\tilde{\psi}_{\mathcal{P}_0}$, (b) $-\Delta\tilde{\psi}_{\mathcal{E}_0, \mathcal{P}_0}$ and (c) $-\Delta\tilde{\psi}_{\mathcal{K}_0, \mathcal{P}_0}$ with $\mathcal{P}_0 \approx 10^8$ in all three cases, $\mathcal{E}_0 = 10^3$ in (b) and $\mathcal{K}_0 = 10$ in (c); (d) the vorticity field $-\Delta\psi(t^*)$ at the time t^* when the largest palinstrophy is attained, i.e., $\mathcal{P}(t^*) = P_{\max}$, in the time dependent problem (3) using the field $-\Delta\tilde{\psi}_{\mathcal{K}_0, \mathcal{P}_0}$ from Figure (c) as the initial data ω_0 .

by the $(\mathcal{K}_0, \mathcal{P}_0)$ -constrained maximizers, but not by the maximizers constrained by \mathcal{P}_0 only (figure 5(b)) is intriguing. We recall that the maximizers found to saturate the instantaneous estimates in 1D and 3D subject to *one* constraint only (on \mathcal{E}) did not saturate the corresponding finite time estimates (Lu & Doering, 2008; Ayala & Protas, 2011). The role of the number of the constraints imposed on the solutions in this type of optimization problems deserves further study.

Moving on to estimate (12) and solutions of the single-constraint optimization problem (18), we observe in figure 2(b) that while $\mathcal{R}_{\mathcal{P}_0}(\tilde{\psi}_{\mathcal{P}_0})$ exhibits a very clean power-law dependence on \mathcal{P}_0 , the associated exponent is in fact significantly less than 2 predicted by estimate (12), cf. table 2. This was in fact to be expected, since upper bound (12) was obtained with the use of Poincaré’s inequality which is saturated only by the eigenfunctions of the Laplacian operator and, as is evident from figure 2(e,h), the maximizing solution $\tilde{\psi}_{\mathcal{P}_0}$ for large \mathcal{P}_0 is quite different from such eigenfunctions. We add that analogous instantaneous estimates in 1D and in 3D were in fact found to be sharp by Lu & Doering (2008), cf. table 1.

We now comment on the structure of the maximizing vorticity fields. In this investigation we focused on periodic solutions possessing the 4-fold rotational symmetry, cf. the assumption in section 5, which lead to lattice-type vorticity distributions. Existence of more exotic optimal vortex states, for example, corresponding in the limit of $\mathcal{P}_0 \rightarrow 0$ to eigenfunctions $\psi_{1,a}(x, y) = \frac{1}{4} \sin(2\pi p x) \sin(2\pi q y)$ and $\psi_{1,s}(x, y) = \frac{1}{4} \sin[2\pi p(x + y)] \sin[2\pi q(x - y)]$ with $p \neq q$ will be explored in the future. We observe that in all three optimization problems, there are two branches of locally maximizing solutions, cf. figures 2, 3 and 4, and they are obtained via continuation from the limiting, for small \mathcal{P}_0 , solutions which were characterized analytically in section 5. In that section we also observed that in the limit of small \mathcal{P}_0 the cubic term in $\mathcal{R}_{\mathcal{P}_0}(\psi)$ vanishes, cf. (37), so that the maximizing fields sustain no stretching of the vorticity gradients. Interestingly, since these limiting maximizers satisfy equation (35a) (which is a special case of $\Delta\psi = F(\psi)$ with a particular $F : \mathbb{R} \rightarrow \mathbb{R}$), they are also steady solutions of the 2D Euler equations (Majda & Bertozzi, 2002). When used as the initial data in a 2D time-dependent Navier-Stokes problem (3), they give rise to the Taylor-Green vortex flow characterized by a purely exponential decay without any nonlinear interactions. We add that 3D generalizations of this flow lead to nontrivial time evolution and have been investigated in the context of the finite-time blow-up problem (Brachet *et al.*, 1983; Brachet, 1991).

As the palinstrophy \mathcal{P}_0 increases, the maximizers in all three optimization problems become localized multipolar vortex structures shown in figures 6(a–c) and featuring a central elongated filament stretched by four satellite vortices: two stronger ones which are closer to the central filament and have the opposite sign, and two weaker ones which are further away and have the same sign as the central filament. In the absence of this central filament, the four satellite vortices would resemble the axial vorticity distribution in the meridional plane intersecting two parallel vortex rings, which was in fact the optimal vortex state found by Lu & Doering (2008, see Figure 4.6a) to saturate the 3D instantaneous estimate (1). This observation offers an interesting analogy to the

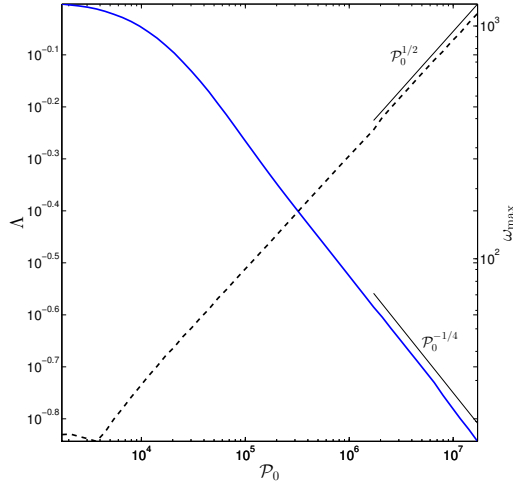


Figure 7: Dependence of (solid) the characteristic length scale $\Lambda = 2\pi\sqrt{\mathcal{K}(\tilde{\psi}_{\mathcal{K}_0, \mathcal{P}_0})/\mathcal{E}(\tilde{\psi}_{\mathcal{K}_0, \mathcal{P}_0})}$ and (dashed) the vorticity magnitude $\omega_{\max} = \|\Delta\tilde{\psi}_{\mathcal{K}_0, \mathcal{P}_0}\|_{L^\infty(\Omega)}$ on \mathcal{P}_0 with $\mathcal{K} = 1$ for the family of maximizers obtained subject to the $(\mathcal{K}_0, \mathcal{P}_0)$ -constraint (cf. figure 4).

3D problem with the presence of the central vortex filament reflecting the difference in the physical quantities maximized in the two problems: vorticity (enstrophy) in 3D versus vorticity gradients (palinstrophy) in 2D. In the limit of large \mathcal{P}_0 , the vortex states corresponding to the two branches appear very similar, except for the rotation by a 45 deg angle. The difference between the cases with one and two constraints is that in the former case the satellite vortices tend to be less localized (which is a consequence of the fact that in that case \mathcal{K}_0 and \mathcal{E}_0 can change freely). With increasing palinstrophy \mathcal{P}_0 , the optimal vortex structures in the single-constraint and $(\mathcal{K}_0, \mathcal{P}_0)$ -constrained cases shrink in a shape-preserving manner with the characteristic dimension Λ of the vortex structure vanishing while its magnitude ω_{\max} grows, so that the vorticity fields can be empirically approximated by the asymptotic formula $\omega_{\mathcal{P}_0}(\mathbf{x}) \sim \omega_{\max} \Pi(\mathbf{x}/\Lambda)$ for some distribution Π independent of \mathcal{P}_0 . Figure 7 shows the dependence of the quantities $\Lambda = 2\pi\sqrt{\mathcal{K}(\tilde{\psi}_{\mathcal{K}_0, \mathcal{P}_0})/\mathcal{E}(\tilde{\psi}_{\mathcal{K}_0, \mathcal{P}_0})}$, cf. (Doering & Gibbon, 1995), and $\omega_{\max} = \|\Delta\tilde{\psi}_{\mathcal{K}_0, \mathcal{P}_0}\|_{L^\infty(\Omega)}$ computed for the upper branch of $(\mathcal{K}_0, \mathcal{P}_0)$ -constrained maximizers on \mathcal{P}_0 with $\mathcal{K}_0 = 1$, cf. figure 4. This data reveals clear power laws $\Lambda \sim \mathcal{P}_0^{-1/4}$ and $\omega_{\max} \sim \mathcal{P}_0^{1/2}$ holding for sufficiently large \mathcal{P}_0 which confirms the scale-independent structure of the maximizing vortex states. Obtaining an analytical characterization of the maximizers $\tilde{\psi}_{\mathcal{P}_0}$ and $\tilde{\psi}_{\mathcal{K}_0, \mathcal{P}_0}$ in the limit $\mathcal{P}_0 \rightarrow \infty$ is an interesting open research problem in mathematical analysis.

Finally, we observe that both families of the maximizing solutions shown in figures 2–4 exhibit an interesting pattern. While for decreasing \mathcal{P}_0 the maximizing solutions approach the Laplacian eigenfunctions with either aligned or staggered arrangement of

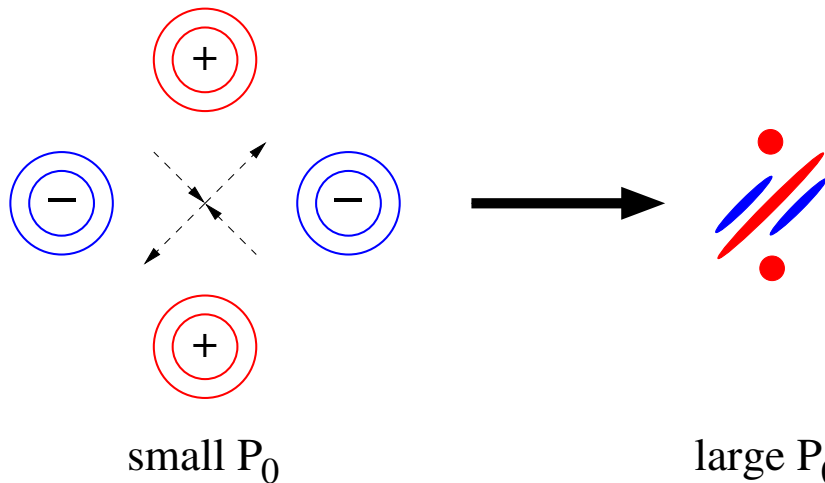


Figure 8: Schematic illustration of the change of the structure of the local maximizers in the staggered arrangement of the vortex cells as \mathcal{P}_0 increases (dashed lines represent the principal directions of stretching and compression).

the vortex cells, cf. (38)–(40) and figure 1, for increasing \mathcal{P}_0 the dominating vortex structure is shifted to the stagnation point of the maximizing fields corresponding to small \mathcal{P}_0 . Furthermore, the dominating vortex structure in the limit of large \mathcal{P}_0 is aligned with the direction of the maximum stretching characterizing the maximizer in the low \mathcal{P}_0 limit, i.e., vertically/horizontally for the aligned arrangement and inclined at the angle of 45 deg for the staggered arrangement. This pattern is schematically illustrated in figure 8.

8 Conclusions and Outlook

In this investigation we addressed a problem which is a part of a broader research program concerning characterization of the maximum growth of certain quadratic quantities in the hydrodynamic systems in different spatial dimensions (cf. table 1). In the context of the 3D Navier-Stokes system these questions are intimately related to the finite-time blow-up problem. Here we focused on the upper bounds for the instantaneous rate of growth of palinstrophy $d\mathcal{P}/dt$ and demonstrated that the key available estimates are in fact sharp and are saturated by families of vorticity fields with nontrivial structure. The optimal vortex states with prescribed energy \mathcal{K}_0 and palinstrophy \mathcal{P}_0 were also found to lead to a time-evolution saturating the finite-time estimate, which is an interesting result highlighting the role the number of constraints may play in this type of problems. Sharpness of finite-time estimates can also be assessed by solving optimization problems defined over *finite* windows of time, as done by Ayala & Protas (2011) for the 1D Burgers equation. It is interesting to see whether such an approach could lead to an improved prefactor in power law (44)(ii). We intend to address this question in the future. As

Estimate	Constraints	Computed Power-Law
$\frac{d\mathcal{P}}{dt} \leq \nu \frac{\mathcal{P}^2}{\mathcal{E}} + \frac{C}{\nu} \mathcal{E} \mathcal{P}$ [cf. (10)]	$\mathcal{E}_0, \mathcal{P}_0$	Not applicable
$\frac{d\mathcal{P}}{dt} \leq \frac{C}{\nu} \mathcal{K}_0^{\frac{1}{2}} \mathcal{P}_0^{\frac{3}{2}}$ [cf. (11)]	$\mathcal{K}_0, \mathcal{P}_0$	$\frac{d\mathcal{P}}{dt} \sim \mathcal{P}_0^{1.49 \pm 0.02}$
$\frac{d\mathcal{P}}{dt} \leq \frac{C}{\nu} \mathcal{P}^2$ [cf. (12)]	\mathcal{P}_0	$\frac{d\mathcal{P}}{dt} \sim \mathcal{P}_0^{1.57 \pm 0.05}$
$\max_{t>0} \mathcal{P}(t) \leq \mathcal{P}_0 + \frac{C}{\nu^2} \mathcal{E}_0^2$ [cf. (14)]	\mathcal{P}_0	$\max_{t>0} \mathcal{P}(t) \sim \mathcal{E}_0^{1.17 \pm 0.02}$
$\max_{t>0} \mathcal{P}(t) \leq \left(\mathcal{P}_0^{1/2} + \frac{C_2}{4\nu^2} \mathcal{K}_0^{1/2} \mathcal{E}_0 \right)^2$ [cf. (15)]	$\mathcal{K}_0, \mathcal{P}_0$	$\max_{t>0} \mathcal{P}(t) \sim \mathcal{E}_0^{1.98 \pm 0.07}$

Table 2: Comparison of the analytical estimates from section 2 and the power-laws discovered by solving the maximization problem in sections 6.1 and 6.2, and the initial-value problems in section 6.3.

regards the present study, an interesting question is how our findings would change if the optimization problems were formulated in an unbounded, rather than periodic, domain. Concerning the research program presented in Introduction, quantifying the maximum finite-time growth of enstrophy in the 3D Navier-Stokes system remains of course the ultimate goal, one which we hope is within reach in the foreseeable future given the currently available computational tools and resources. An interesting intermediate step is to consider similar questions for the 2D surface quasi-geostrophic (SQG) equation

$$\frac{\partial \theta}{\partial t} + (\mathbf{v} \cdot \nabla) \theta = -\nu (-\Delta)^\alpha \theta, \quad (45)$$

where $\mathbf{v} = \nabla^\perp (-\Delta)^{-1/2} \theta$ and $0 \leq \alpha \leq 1$. As is well known (Kiselev *et al.*, 2006), see also Scott (2011), solutions of (45) do exhibit finite-time blow-up in the subcritical case $\alpha < 1/2$. Therefore, aside from its own intrinsic interest, this problem represents a useful testbed for development and validation of methods to track singular solutions in the 2D setting which is more computationally manageable than the full 3D Navier-Stokes problem.

We wish to emphasize that the research methodology developed here, relying on a systematic characterization of the extremal behavior, appears applicable to other related open problems in the field of theoretical fluid dynamics. An example of such a problem is obtaining sharp bounds on the Nusselt number in the Rayleigh-Bénard convection. There are also similar problems related to mixing.

Acknowledgements

The authors are indebted to Charles Doering and Evelyn Lunasin for many enlightening discussions concerning the research problems studied in this work and, in particular, for

providing estimates (10) and (14). This research was funded through an Early Researcher Award (ERA) and the computational time was made available by SHARCNET.

A Derivation of Estimates (11) and (15)

A key element necessary to derive the upper bound in (11) is the following estimate for the L_∞ norm of doubly-periodic functions $u : \Omega \rightarrow \mathbb{R}$

$$\|u\|_\infty \leq C \|u\|_2^{1/2} \|\Delta u\|_2^{1/2}, \quad (46)$$

where $C > 0$, which follows from Sobolev Interpolation Theorem (Adams & Fournier, 2005). A calculation showing that for $\Omega = [0, 1]^2$, $C = 1/\sqrt{\pi}$ can be found in Ayala (2013). This estimate can be generalized for the case of vector-valued functions $\mathbf{u} : [0, 1]^2 \rightarrow \mathbb{R}^2$ by noticing that $\|\mathbf{u}\|_2^2 = \sum_i \|u_i\|_2^2 \Rightarrow \|u_i\|_2^2 \leq \|\mathbf{u}\|_2^2$ for $i = 1, 2$. Hence

$$\begin{aligned} \|\mathbf{u}\|_\infty &= \max_i \{\|u_i\|_\infty\} \\ &\leq \max_i \left\{ C \|u_i\|_2^{1/2} \|\Delta u_i\|_2^{1/2} \right\} \\ &\leq \max_i \left\{ C \|\mathbf{u}\|_2^{1/2} \|\Delta \mathbf{u}\|_2^{1/2} \right\} \end{aligned}$$

Therefore, in the case of vector-valued functions we have

$$\|\mathbf{u}\|_\infty \leq C \|\mathbf{u}\|_2^{1/2} \|\Delta \mathbf{u}\|_2^{1/2}. \quad (47)$$

We notice that the estimate depends only on the L_2 norms of the function and some of its second derivatives. To obtain estimate (11) from Section 2, we write the rate of growth of palinstrophy as, cf. (9),

$$\frac{d\mathcal{P}}{dt} = -\nu \int_\Omega |\Delta \omega|^2 d\Omega + \int_\Omega \mathbf{u} \cdot \nabla \omega \Delta \omega d\Omega. \quad (48)$$

The second term on the RHS in (48) can be upper-bounded as

$$\begin{aligned} \left| \int_\Omega \mathbf{u} \cdot \nabla \omega \Delta \omega d\Omega \right| &\leq \|\mathbf{u} \cdot \nabla \omega\|_2 \|\Delta \omega\|_2 \\ &\leq \|\mathbf{u}\|_\infty \|\nabla \omega\|_2 \|\Delta \omega\|_2 \\ &\leq C \|\mathbf{u}\|_2^{1/2} \|\Delta \mathbf{u}\|_2^{3/2} \|\Delta \omega\|_2, \end{aligned}$$

where inequality (47) has been used together with the Cauchy-Schwarz inequality and the fact that $\|\nabla \omega\|_2 = \|\Delta \mathbf{u}\|_2$. The application of Young's inequality

$$ab \leq \frac{\beta^p a^p}{p} + \frac{b^q}{q \beta^q}$$

to (48) with $p = q = 2$ and $\beta^2 = (2\nu)^{-1}$ yields

$$\begin{aligned}\frac{d\mathcal{P}}{dt} &\leq -\nu\|\Delta\omega\|_2^2 + \frac{C^2}{4\nu}\|\mathbf{u}\|_2\|\Delta\mathbf{u}\|_2^3 + \nu\|\Delta\omega\|_2^2 \\ &\leq \frac{C^2}{4\nu}\|\mathbf{u}\|_2\|\Delta\mathbf{u}\|_2^3.\end{aligned}\tag{49}$$

Finally, inequality (49) can be rewritten in terms of energy and palinstrophy as, cf. (11),

$$\frac{d\mathcal{P}}{dt} \leq \frac{C^2}{\nu}\mathcal{K}^{1/2}\mathcal{P}^{3/2}.\tag{50}$$

From Navier-Stokes system (3) it follows that $d\mathcal{K}/dt = -2\nu\mathcal{E}$ and $d\mathcal{E}/dt = -2\nu\mathcal{P}$. Therefore, $\mathcal{K}(t) < \mathcal{K}(0) = \mathcal{K}_0$ and $\mathcal{E}(t) < \mathcal{E}(0) = \mathcal{E}_0$ for all $t > 0$. Estimate (50) can be transformed as

$$\begin{aligned}\frac{d\mathcal{P}}{dt} &\leq \frac{C^2}{\nu}\mathcal{K}_0^{1/2}\mathcal{P}^{3/2} \quad \implies \\ \mathcal{P}^{-1/2}\frac{d\mathcal{P}}{dt} &\leq \frac{C^2}{\nu}\mathcal{K}_0^{1/2} \quad \implies \\ \frac{d}{dt}(2\mathcal{P}^{1/2}) &\leq \frac{C^2}{\nu}\mathcal{K}_0^{1/2}.\end{aligned}$$

Integrating the last inequality over time and using the fact that

$$\int_0^t \mathcal{P}(s) ds = \frac{\mathcal{E}(0) - \mathcal{E}(t)}{2\nu} \leq \frac{\mathcal{E}_0}{2\nu},$$

it is possible to obtain

$$\mathcal{P}(t) \leq \left[\mathcal{P}_0^{1/2} + \left(\frac{C}{2\nu} \right)^2 \mathcal{K}_0^{1/2} \mathcal{E}_0 \right]^2.\tag{51}$$

This upper bound is valid for all $t > 0$ and the right-hand side depends only on the initial values of energy, enstrophy and palinstrophy. Estimate (15) is then obtained by taking the maximum over time on the LHS in (51).

References

- ADAMS, R. A. & FOURNIER, J. F. 2005 *Sobolev Spaces*. Elsevier.
- AYALA, D. 2013 On the maximal growth of H^s norms in a hydrodynamic system. PhD thesis, McMaster University, in preparation.
- AYALA, D. & PROTAS, B. 2011 On maximum enstrophy growth in a hydrodynamic system. *Physica D* **240**, 1553–1563.

- AYALA, D. & PROTAS, B. 2013 Vortices, maximum growth and the problem of finite-time singularity formation. In preparation.
- BRACHET, M. E. 1991 Direct simulation of three-dimensional turbulence in the Taylor–Green vortex. *Fluid Dynamics Research* **8**, 1–8.
- BRACHET, M. E., MEIRON, D. I., ORSZAG, S. A., NICKEL, B. G., MORF, R. H. & FRISCH, U. 1983 Small-scale structure of the Taylor–Green vortex. *Journal of Fluid Mechanics* **130**, 411–452.
- DASCALIUC, R., FOIAS, C. & JOLLY, M. S. 2010 Estimates on enstrophy, palinstrophy, and invariant measures for 2D turbulence. *Journal of Differential Equations* **248**, 792–819.
- DOERING, C. R. 2009 The 3D Navier-Stokes problem. *Annual Review of Fluid Mechanics* pp. 109–128.
- DOERING, C. R. & GIBBON, J. D. 1995 *Applied Analysis of the Navier-Stokes Equations*. Cambridge University Press.
- DOERING, C. R. & LUNASIN, E. 2011 Limits on palinstrophy growth for solutions of the two-dimensional Navier–Stokes equations. Personal communication.
- EDWARDS, W. S., TUCKERMAN, L. S., FRIESNER, R. A. & SORENSEN, D. C. 1994 Krylov method for the incompressible Navier–Stokes equation. *Journal of Computational Physics* **110**, 82–102.
- FEFFERMAN, C. L. 2000 Existence and smoothness of the Navier-Stokes equation. http://www.claymath.org/millennium/Navier-Stokes_Equations/navierstokes.pdf.
- FOIAS, C. & TEMAM, R. 1989 Gevrey class regularity for the solutions of the Navier–Stokes equations. *Journal of Functional Analysis* **87**, 359–369.
- GIBBON, J. D., BUSTAMANTE, M. & KERR, R. M. 2008 The three-dimensional Euler equations: singular or non-singular? *Nonlinearity* **21**, 123–129.
- GRAFKE, T., HOMANN, H., DREHER, J. & GRAUER, R. 2008 Numerical simulations of possible finite-time singularities in the incompressible Euler equations: comparison of numerical methods. *Physica D* **237**, 1932–1936.
- GUNZBURGER, M. D. 2003 *Perspectives in Flow Control and Optimization*. SIAM.
- HOU, T. Y. 2009 Blow-up or no blow-up? a unified computational and analytic approach to 3D incompressible Euler and Navier–Stokes equations. *Acta Numerica* pp. 277–346.
- KERR, R. M. 1993 Evidence for a singularity of the three-dimensional, incompressible Euler equations. *Phys. Fluids A* **5**, 1725–1746.

- KISELEV, A., NAZAROV, F. & VOLBERG, A. 2006 Global well-posedness for the critical 2D dissipative quasi-geostrophic equation. *Invent. math.* **167**, 445–453.
- KREISS, H. & LORENZ, J. 2004 *Initial-Boundary Value Problems and the Navier-Stokes Equations, Classics in Applied Mathematics*, vol. 47. SIAM.
- LU, L. 2006 Bounds on the enstrophy growth rate for solutions of the 3D Navier-Stokes equations. PhD thesis, University of Michigan.
- LU, L. & DOERING, C. R. 2008 Limits on enstrophy growth for solutions of the three-dimensional Navier–Stokes equations. *Indiana University Mathematics Journal* **57**, 2693–2727.
- LUENBERGER, D. 1969 *Optimization by Vector Space Methods*. John Wiley and Sons.
- MAJDA, A. J. & BERTOZZI, A. L. 2002 *Vorticity and Incompressible Flow*. Cambridge University Press.
- MATSUMOTO, T., BEC, J. & FRISCH, U. 2008 Complex-space singularities of 2D Euler flow in lagrangian coordinates. *Physica D* **237**, 1951–1955.
- OHKITANI, K. 2008 A miscellany of basic issues on incompressible fluid equations. *Non-linearity* **21**, 255–271.
- OHKITANI, K. & CONSTANTIN, P. 2008 Numerical study of the eulerian–lagrangian analysis of the Navier-Stokes turbulence. *Phys. Fluids* **20**, 1–11.
- ORLANDI, P., PIROZZOLI, S. & CARNEVALE, G. F. 2012 Vortex events in Euler and Navier-Stokes simulations with smooth initial conditions. *Journal of Fluid Mechanics* **690**, 288–320.
- PELINOVSKY, D. 2012a Enstrophy growth in the viscous Burgers equation. *Dynamics of Partial Differential Equations* **9**, 305–340.
- PELINOVSKY, D. 2012b Sharp bounds on enstrophy growth in the viscous Burgers equation. *Proceedings of Royal Society A* **468**, 3636–3648.
- PELZ, R. B. 2001 Symmetry and the hydrodynamic blow-up problem. *Journal of Fluid Mechanics* **444**, 299–320.
- POUQUET, A., LESIEUR, M., ANDRÉ, J. C. & BASDEVANT, C. 1975 Evolution of high Reynolds number two-dimensional turbulence. *Journal of Fluid Mechanics* **72**, 305–319.
- PROTAS, B., BABIANO, A. & KEVLAHAN, N. K. R. 1999 On geometrical alignment properties of two-dimensional forced turbulence. *Physica D* **128**, 169–179.

- PROTAS, B., BEWLEY, T. & HAGEN, G. 2004 A comprehensive framework for the regularization of adjoint analysis in multiscale PDE systems. *Journal of Computational Physics* **195**, 49–89.
- RABIN, S. M. E., CAULFIELD, C. P. & KERSWELL, R. R. 2012 Variational identification of minimal seeds to trigger transition in plane Couette flow. *Journal of Fluid Mechanics* **712**, 244–272.
- RUSZCZYŃSKI, A. 2006 *Nonlinear Optimization*. Princeton University Press.
- SCOTT, R. K. 2011 A scenario for finite-time singularity in the quasigeostrophic model. *Journal of Fluid Mechanics* **687**, 492–502.
- SIEGEL, M. & CAFLISCH, R. E. 2009 Calculation of complex singular solutions to the 3D incompressible Euler equations. *Physica D* **238**, 2368–2379.
- SULEM, C., SULEM, P. L. & FRISCH, H. 1983 Tracing complex singularities with spectral methods. *Journal of Computational Physics* **50**, 138–161.
- TRAN, CH. V. & DRITSCHEL, D. G. 2006 Vanishing enstrophy dissipation in two-dimensional Navier–Stokes turbulence in the inviscid limit. *Journal of Fluid Mechanics* **559**, 107–116.